2019

High-Pressure Studies on Borosilicate and Bulk Metallic Glasses

Kathryn Jinae Ham
University of Alabama at Birmingham

HIGH-PRESSURE STUDIES ON BOROSILICATE AND BULK METALLIC GLASSES

by

KATHRYN JINAE HAM

YOGESH K. VOHRA, COMMITTEE CHAIR
SHANE A. CATLEDGE
ANDREW A. WERESZCZAK
ROSTISLAV HRUBIAK
CHENG-CHIEN CHEN

A DISSERTATION

Submitted to the graduate faculty of The University of Alabama at Birmingham,
in partial fulfillment of the requirements for the degree of
Doctor of Philosophy

BIRMINGHAM, ALABAMA

2019

HIGH-PRESSURE STUDIES ON BOROSILICATE AND BULK METALLIC GLASSES

KATHRYN JINAE HAM

PHYSICS

ABSTRACT

Multi-angle energy-dispersive X-ray diffraction (EDXD) and white-beam radiography studies were conducted on a borosilicate glass sample (17.6% B_2O_3) to 13.7 GPa in a Paris-Edinburgh (PE) press at Beamline 16-BM-B, HPCAT, The Advanced Photon Source, Argonne National Laboratory. The measured structure factor *S(q)* to q = 19 $Å^{-1}$ was used to determine internuclear bond distances between various species of atoms contained in the glass sample. Bond distances for Si-O, O-O, and Si-Si were determined from the reduced pair distribution function *G(r)* and were measured as a function of pressure. The sample height, as determined via white-beam radiography, showed an overall uniaxial compression of 22.5% at 13.7 GPa and a 10.6% permanent compaction after decompression to ambient conditions. Raman spectroscopy of the pressure recovered borosilicate glass sample as compared to the bulk starting material shows blue-shift and changes in intensities and widths of the Raman bands associated with four-coordinated boron and silicate rings.

Density measurements of borosilicate glasses of varying B_2O_3 percentages revealed that a higher B_2O_3 percentage leads to a greater volume change after compression to ~12 GPa.

A high pressure, high temperature study on Vit 106a bulk metallic glass reveals a large volume collapse at 460°C via X-ray radiography, which is indicative of

crystallization. There are five equilibrium crystalline phases for the fully crystallized sample at 800°C: ZrCu, Zr_2Cu, Zr_3Al_2, Zr_4Al_3, and Zr_2Ni.

The effect of pressure and heating rate on crystallization temperature was investigated for Vit 106a. Three different heating rates were studied: 1.2°C/min, 2.4°C/min, and 6.0°C/min. A trend is seen where an increase in heating rate leads to an increase in crystallization temperature, and for each heating rate there is a positive correlation between pressure and crystallization temperature in a low-pressure range from ambient to ~3-4 GPa, and a negative correlation between pressure and crystallization temperature in a range from 3-4 GPa – 6.5 GPa.

Keywords: high-pressure, physics, borosilicate glass, bulk metallic glass, Paris-Edinburgh press, diamond anvil cell

DEDICATION

I would like to dedicate this work to my incredible fiancé, Dr. Jason Burke for all of his unconditional love and support. I am so lucky to have such a supportive and caring partner for life. I would like to dedicate this work to my parents, Jay and Colleen Ham; my sister, Caroline Ham; and the rest of my incredible family and wonderful friends for their endless love, constant support, and continual encouragement in this and all aspects of life. Most of all to my parents who have, without doubt, made the greatest, most profound, and an unquestioningly positive impact on my life. For providing me with 25 years filled to the brim with unconditional love, support in all endeavors, endless happy memories and opportunities, and of course for filling my life with delicious daily culinary masterpieces (à la Chef Jay). Mom and Dad, you guys are the most selfless, hardworking, and loving parents and I want to say thank you for everything you have provided, everything you have sacrificed, and everything you have done for me with to get me to this point in my life today. To Caroline for always being my toughest critic, but also my favorite friend. You've always been there for me for the highs and the lows, with all the patience and compassion in the world. To Grandma for showing me that it truly is a wonderful life. To my friends for showing me that you can work hard, but play harder. With infinite love, I say thank you to everyone in my life for everything.

Bigger than the airplanes; wider than the skies…

ACKNOWLEDGEMENTS

I acknowledge support from the US Department of Education, Graduate Assistance in Areas of National Need (GAANN) program under Award P200A150001. Partial support of this research was provided by the U.S. Army Research Office under Grant No. W911NF-15-10614. Portions of this work were performed at Beamline 16-BM-B, HPCAT (High Pressure Collaborative Access Team), Advanced Photon Source (APS), Argonne National Laboratory. HPCAT operations are supported by DOE-NNSA under Award No. DENA0001974 and DOE-BES under Award No. DE-FG02-99ER45775, with partial instrumentation funding by NSF. APS is supported by DOE-BES, under Contract No. DEAC02-06CH11357. Portions of this work were performed at HPCAT (Sector 16), The Advanced Photon Source (APS), Argonne National Laboratory. I would like to thank and acknowledge Andrew A. Wereszczak and Emily F. Steiner for conducting DSC measurements conducted on Vit 106a. I would like to thank and acknowledge Parimal Patel and Steven Kilczewski for the fabrication of the borosilicate glass samples. I would like to thank and acknowledge Curtis Kenney-Benson for making the sample assembly for the PE press as well as machining the borosilicate glass samples studied in the PE press.

TABLE OF CONTENTS

Page

LIST OF TABLES

Table *Page*

LIST OF FIGURES

Figure *Page*

LIST OF ABBREVIATIONS

θ	diffraction angle
λ	wavelength
υ	frequency
$\bar{\upsilon}$	wavenumber
APS	Advanced Photon Source
BMG	bulk metallic glass
B_0	bulk modulus
B_0'	first derivative of the bulk modulus
c	speed of light
c_i	the atomic factor
d	d-spacing
E	energy
EDXD	energy-dispersive X-ray diffraction
FCC	face centered cubic
$f_i(q)$	atomic scattering factor
Ge-SSD	germanium solid state detector
G(r)	reduced pair distribution function
HPCAT	High Pressure Collaborative Access Team
n	positive integer
PE	Paris-Edinburgh
S(q)	structure factor
q	scattering vector

INTRODUCTION

Motivations

Borosilicate glass for use in transparent armor systems has been investigated by the U.S. Army Research Laboratory [1]. In general, glass has been chosen due to its low cost, wide availability, and valuable mechanical properties like stiffness and hardness [1,2]. Two types of glass had been considered: a borosilicate glass and a soda-lime silica glass [1]. In general, borosilicate glass is comprised largely of SiO_2 (~75% wt) with the addition of B_2O_3 as the second largest component [2]. Soda-lime glass, in general, also consists mostly of SiO_2 with the addition of Na_2O and CaO [2]. In both of these glasses various other oxides, such as Na_2O, K_2O, or Al_2O_3 are added in minute amounts, as compared to the two main components in each glass [2]. When comparing two commercially available samples: Borofloat ® borosilicate glass and Starphire ® soda-lime silicate float glass, Borofloat ® was determined to have smaller bulk, elastic, and shear moduli, which means that Borofloat ® could have desirable characteristics such as a deeper penetration depth from a ballistic event, the maximum stress will be smaller for a given contact force, and the pressure to cause onset densification will be lower than for Starphire ® [2]. Borosilicate glass also has a 10-11% lower density as compared to soda-lime glass, a sought after property for the material used in the transparent armor systems [1,2].

The specific borosilicate glass sample explored in this thesis work is investigated on both a micro (on the order of Å) and macro (on the order of mm) scale. On the micro scale, multi-angle energy-dispersive X-ray diffraction and Raman spectroscopy have been

used to investigate how the various atomic bonds within the sample change under a high-pressure environment, and to investigate any permanent deformation in the atomic bond lengths after pressure is released. On the macro scale, white-beam radiography has been used to investigate direct changes to the glass sample's bulk as pressure is increased, and to investigate any permanent deformation in the sample's volume after pressure is released. Three samples with varying B_2O_3 contents were investigated to determine the effect that the B_2O_3 content had on permanent deformation of the sample after being exposed to high pressure conditions.

Borosilicate Glass Overview

Borosilicate Glass History

In the late 1800's German physicist, Ernst Abbe, and chemist, Otto Schott, worked together at the forefront of glass science with the help of microscope maker, Carl Zeiss; working to learn more about the properties of glass [3]. At the time of the beginning of Schott and Abbe's work, no outstanding scientific theories existed to explain the variance in the properties of glass which resulted from slight variations in the composition of ingredients; thus, much of this duo's work relied heavily on a trial-and-error process [3]. Schott would make glass of differing compositions, and Abbe would measure the results [3]. If the properties of the glass seemed to improve, Schott and Abbe would send the sample to Zeiss for final grinding and polishing, where he would disclose the performance of the finished lens back to Schott and Abbe [3]. In 1884, the Jena firm of Schott and Genossen emerged, and by 1886 the first publication of the catalog from

"Glastechnisches Laboratorium, Schott und Genossen," was released and contained 44 different optical glasses [3].

The first borosilicate glass was made in the late 1800s by Abbe and Schott, who were the first to add boron compounds in large concentrations, first to optical glasses and next to laboratory apparatus glass [3]. Schott's continued efforts lead to the observation that boron's addition to silicate glass produced a glass with notable resistance to boiling water, a valuable property for improved laboratory glassware [3]. Further studies found that the addition of boron trioxide (B_2O_3) to silicate glass proved the most effective additive in the reduction of the coefficient of thermal expansion [3]. Schott Borofloat ® 33, a presently commercially available borosilicate glass, whose derivatives are studied in this present research, is produced by a float process. The float process, first successfully used in 1959, moves a continuous ribbon of glass from the melting furnace onto an enclosed bath of completely flat molten tin, which yields a sheet of glass that is free of irregularities and has no need for grinding or polishing [4].

Borosilicate Glass Properties

Borosilicate glass, comprised largely of silica (SiO_2) and B_2O_3 network formers, has many attractive properties such as low cost, wide availability, excellent durability, resistance to heat and valuable mechanical properties such as stiffness and hardness [1,5–7]. These properties make borosilicate glass a prominent candidate for protective transparent armor systems (Figure 1) [1,2]. An additional benefit of borosilicate glass over other alternatives, such as soda-lime silicate glass, is ~ 10-11% lower density due to a larger content of B_2O_3 [1,2]. Optically, permanently transparent borosilicate glass, Borofloat ®

33 has outstanding transmission behavior, attributed to use of low impurity materials and an optimized glass manufacturing process [7].

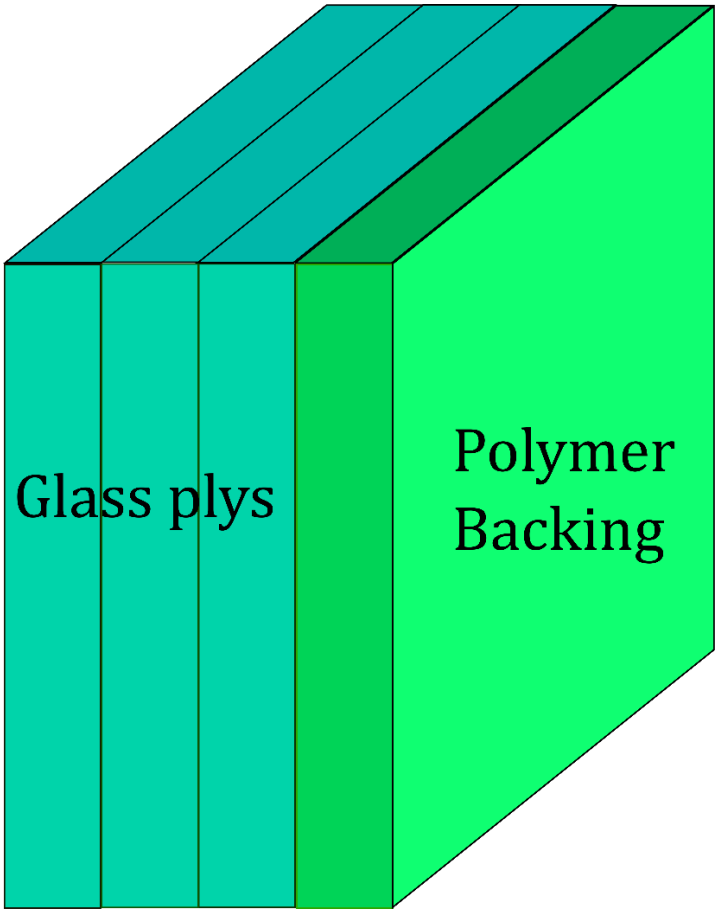

Figure 1. Illustration of transparent armor with three layers of glass ply and one polymer backing layer.

Bulk Metallic Glass Overview

Bulk Metallic Glass History

A new class of materials was initiated with the creation of the first bulk metallic glass, $Au_{75}Si_{25}$ by Duwez, *et. al.* at Caltech in 1960 [8]. This amorphous metal was created by quickly quenching from 1300°C to room temperature at rates of 10^5-10^6 K/s and was

characterized amorphous by X-ray diffraction of a flake with a 0.2 mm^2 area and ~ 10 μm thickness [8]. In 1974 Chen created the first millimeter scale bulk metallic glass, a three-component Pd-Cu-Si alloy in the form of millimeter diameter rods, using a critical cooling rate of 10^3 K/s [9]. This work was significant since it increased the size of the bulk metallic glass sample and lowered the critical cooling rate, as compared to its predecessor, the two-component Au-Si alloy [8,9]. The next milestone accomplishment occurred in 1982 when Turnbull *et. al.* created a Pd-Ni-P bulk metallic glass sample on the scale of centimeters, with a critical cooling rate on the order of 10 K/s [10]. A step forward in achieving a bulk metallic glass with a lower critical cooling rate and a larger size. Over the course of a decade, the trend of creating BMGs from expensive metals such as Au, Pd, and Pt (1967, Au-Si-Ge [11], 1974, Pd-Cu-Si [9]; 1975, Pt-Ni-P [12]) was traded for a trend of creating BMGs from less expensive metals such as Zr, Ni, and Ln (Lanthanide metal) (1989, Al-La-Ni [13]; 1990, Zr-Al-Ni [14]; 1991, Zr-Al-TM (TM = Co, Ni, Cu) [15]. A decade later BMGs transitioned into using even more inexpensive metals such as Fe and Cu (2001, Ti-Zr-Ni-Cu [16]; 2001, Fe-(Zr, Hf, Nb)-B [17]). Generally, the goal throughout the history of bulk metallic glass creation was to find materials that were made from less expensive elements, could be produced in larger sizes, and had lower critical cooling rates.

Bulk Metallic Glass Properties

The glass forming ability (GFA) in a bulk metallic glass increases with the number of constituents in the material due to the "confusion principle," where the competing crystalline phases within the material are destabilized during cooling as the number of mismatched atomic components are increased [18]. In 2000, Inoue *et. al.* established a

basis of three rules to describe the glass forming ability in bulk metallic glasses: 1) the system has more than 3 elements, 2) there is a significant difference in the atomic size of the different elements, where there is at least a 12% size ratio difference between each of the three more prevalent atomic species, and 3) the three main components should have negative heats of mixing [19]. Compounds satisfying all three rules will have a more favorable thermodynamic, kinetic and microstructure development for glass formation over crystal formation [19]. When there is a system with more than 3 elements, this leads to an increase in the complexity of the system which gives the crystalline system less of an energetic advantage to form, as there are various crystalline phases of differing sizes competing to form [20]. When there is a greater atomic radius mismatch between elements, $\Delta r/r$ > 12% there is a smaller free volume and a higher packing density within the liquid system, as compared to metallic melts [20]. The energy barrier at the liquid-solid interface is increased when there is a negative heat of mixing between the majority elements in the BMG [20]. A negative heat of mixing also decreases the atomic diffusivity, which slows the crystal nucleation rate in the BMG, making it more difficult for the crystal phases to form [20].

The most valuable properties of BMGs are their strength, which is twice that of stainless steel; a high hardness which makes them ideal for surface coatings; toughness, which makes BMGs more fracture resistant than ceramics; and good elasticity, with high yield strength [20]. Since the structure of BMGs is tightly packed, it is more difficult to displace atoms, leading to less energy absorbed during a stress-induced deformation event [20]. This leads to a material that can return to its original shape more easily by rebounding elastically [20].

Bulk Metallic Glass Uses

The wide variety of uses of BMGs extends over various fields, from biomedical to engineering uses, to commercial products, to military applications. Zr-based BMGs have been investigated for the use as biomaterials due to their mechanical and wear properties as well as their bio-corrosion resistance [21]. Due to their potential in biomedical applications (femur implant [22], orthopedic repair and replacement [23], dental implants [24]), there have been many studies conducted looking into the biocompatibility and cytotoxicity of Zr-based BMGs. The Zr-based BMGs have a notable advantage over currently used biocompatible materials: commercially pure Ti and Ti-6Al-4V in regard to Young's modulus, fracture toughness, elastic limit, and corrosion resistance [24]. The Zr-based BMG that has been investigated for use as a dental implant material, $Zr_{61}Ti_2Cu_{25}Al_{12}$ is free from toxic elements like Ni, Co, and Be and also exhibits valuable mechanical properties such as a low Young's modulus, E = 83 GPa and a high fracture toughness, K_{1C} = 130 Mpa$\sqrt{m}$, where as Ti has a Young's modulus of E = 110 GPa [24]. A lower Young's modulus is valuable, as human bone has a Young's modulus of 10 – 30 GPa and the greater the difference between bone and the implant material the greater the possibility of implant rejection [24].

While BMGs offer a range of desirable mechanical qualities, one perceived limitation has been their lower fatigue resistance, as compared to crystalline alloys and metals [25]. A highly fatigue resistant Zr-based BMG, $Zr_{52.5}Cu_{17.9}Ni_{14.6}Al_{10}Ti_5$ has been investigated as a prime candidate for future applications requiring good mechanical fatigue resistance [25]. Vitreloy 1, $Zr_{41.2}Be_{22.5}Ti_{13.8}Cu_{12.5}Ni_{10}$, a Zr-based BMG has also been used

to make high-performance golf clubs, where the ability to efficiently return elastic energy is important to the club's performance [26].

Along with biomedical and engineering applications, BMGs have been investigated for use in military application. Tungsten (W) with a BMG matrix has been studied for use as kinetic energy penetrator material to try and replace the commonly used depleted-uranium-based alloys due to post use environmental cleanup concerns [27,28]. A kinetic energy penetrator is designed as an anti-armor warhead, where armor is pierced using kinetic energy instead of an explosive [29]. In order for a kinetic energy penetrator to be effective, it must be made out of a high-density material, fired at a high velocity, and have its force concentrated into a relatively small impact area [29]. Depleted uranium has a high density of ~19 grams/cm^3, which is much higher than typical Zr-based BMGs which have densities ~6.7 grams/cm^3, which leads to the necessity to add a heavy metal such as W, with a density of 19.3 grams/cm^3, to a BMG matrix in order to achieve performance similar to that of depleted uranium [28,30].

In the past few decades since the first BMG was created the number of applications has grown significantly. Bulk metallic glasses have been used in a wide range of biomedical, engineering, commercial, and military applications. Although they have been widely regarded for their toughness, high yield strength, and hardness, the current drawback remains where the material growth is still limited to a few centimeters. While much progress has been made since the first bulk metallic glass was created in 1960, there are still more discoveries to be made in this relatively new field of study: new bulk metallic glasses that will have slower critical cooling rates, can be made into larger sizes, and fabricated for different applications.

In this research, a Zr-based BMG is investigated to determine structural response in a high-pressure, high-temperature environment; the effect that high pressure and temperature have on the crystallization temperature; and if there is existence of a critical heating rate at which the sample can go from solid to melt without devitrification.

White Beam X-Ray Diffraction Overview

X-Ray Diffraction History

X-rays were first discovered by Wilhelm Röntgen in 1895 and used to produce radiographs, captured on photographic film when placed behind an object with an incoming X-ray source from the other side [31]. These radiographs produce pictures based on the varying density of the object studied, where portions of the object with a lower density correspond to brighter sections on the radiograph [31]. However, it was not until 1912 that X-rays were used to probe the structure of crystalline materials. Max von Laue, a German physicist, was the first to conduct experiments using X-rays to look for a diffraction pattern in a crystalline material to confirm theories stating that crystals form in a periodic arrangement [31]. Diffraction patterns occur when X-rays are scattered off of different planes of atoms and constructively interfere. In 1912 William Lawrence Bragg determined a formula to relate the wavelength of the incident X-rays to the distance between the atomic layers and the angle of incident X-rays [31]. Since the first use of X-rays on a sample of copper sulfate by Max von Laue in 1912, much progress and innovation have occurred in the field [31].

X-Ray Diffraction Techniques

X-ray diffraction is a technique used for determining the atomic or molecular structure of materials [32]. When X-ray radiation is directed onto a sample, the X-rays are scattered by the electrons in the material (Figure 2) [32]. Interference occurs when there is a superposition of two or more of the scattered waves, and diffraction is the result of the constructive interference of more than one scattered wave [32].

For a crystalline sample, with periodic, long-range order, constructive interference, or diffraction, can be described by Bragg's law:

$$n\lambda = 2d \cdot sin(\theta) \quad (1)$$

Where n is a positive integer, λ is the X-ray wavelength, d is the distance between crystal lattice planes (d-spacing), and θ is the diffraction angle [32]. Using Bragg's law, three main diffraction methods can be explored: Laue method, which looks at diffraction from a single crystal sample with white beam radiation at a fixed angle; rotating crystal method, which uses a monochromatic X-ray source (fixed wavelength) and a variable angle θ on a single crystal sample; and powder method, which uses a monochromatic X-ray source and a variable θ value on a powder sample (Figure 2) [31].

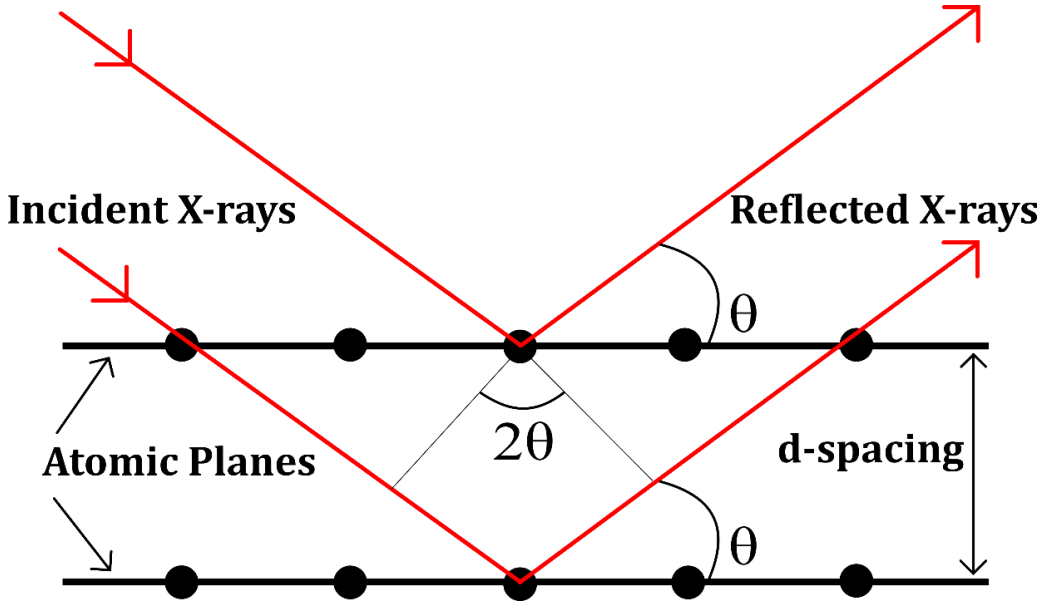

Figure 2. Schematic representation of the diffraction of X-rays in a crystalline material.

X-Ray Diffraction on Glasses

One application of X-ray diffraction involves the use of a Paris-Edinburgh cell to compress materials to gigapascal high pressures, and probe different materials with X-rays to discover how the materials' structures changes with pressure [33]. Gold can be used as a pressure standard for this type of research, as it has a relatively simple Face Centered Cubic (FCC) crystal structure and its equation of state is well understood to high pressures [34,35].

Multi-angle energy-dispersive white-beam X-ray diffraction (EDXD), an analytical technique for characterizing materials, is used to measure the structures of liquids and solids at high pressures and temperatures [33]. EDXD relies on a fixed scattering angle, works directly in reciprocal space, and collects the entire spectrum of diffraction radiation simultaneously. The fixed scattering angle with EDXD means that only one entrance and

exit space are needed to study the sample, which makes this method useful for studying materials in extreme environments such as high temperature and pressure. Since the spectrum is collected simultaneously, this make EDXD suitable for studying materials in states that exist for a short amount of time or change rapidly.

Since amorphous materials, such as glass, do not have a periodic structure or long-range atomic order, there are only broad scattering features seen from X-ray diffraction [36]. Multi-angle EDXD utilizes white X-ray radiation, with energy *E* and scattering angle *2θ* [33,37]. The scattering vector *q* is defined as:

$$q = \frac{4\pi \cdot E}{12.3984} \sin(\theta) \tag{2}$$

The Faber - Ziman liquid structure factor, which is the diffraction pattern that has been corrected for experimental artifacts and normalized, to $\langle S(q) \rangle = 1$, is defined as [33,37]:

$$S(q) = \frac{I_{coh}(q) - <f^2(q)>}{<f(q)>^2} + 1 \tag{3}$$

Where $I_{coh}(q)$ is the coherent scattering from the sample, $< f(q) > \equiv \sum_i c_i f_i(q)$, c_i is the atomic factor, and $f_i(q)$ is the atomic scattering factor [33]. The reduced pair distribution factor *G(r)* is obtained as [33,37]:

$$G(r) = \frac{2}{\pi} \int_{q_{min}}^{q_{max}} q[S(q) - 1] \sin(qr)\, dq \tag{4}$$

Where q_{max} is the maximum measured scattering vector, q_{min} is the minimum measured scattering vector, q is the scattering vector [33,37]. *G(r)* has peaks at a distance *r* (Å), which correspond with a high probability to the separation distance between various

pairs of atoms [37]. The function oscillates around zero, asymptotes to zero for high r values, and tends towards zero as $r \rightarrow 0$, for $r <$ "hard sphere limit," with a slope of $-4\pi\rho_0$, where ρ_0 is the average number density of the material [37].

Raman Spectroscopy Overview

Raman Spectroscopy History

Raman spectroscopy, a spectroscopic technique used to identify compounds, relies on the inelastic scattering of mono-chromatic light to observe vibrational or rotational modes in the system [38,39]. The idea of the inelastic scattering of light was first proposed by Smekal in 1923 [40]. Raman and Krishnan observed the first experimental evidence of this phenomena in liquids in 1928 [41].

Raman Spectroscopy Techniques

The interaction of light with matter results in either the absorption, scattering, or non-interaction of photons [39]. Absorption of the incident photon occurs when its energy corresponds to the energy gap between the ground state and an excited state of the molecule, and the molecule is promoted to the excited energy state [39]. Absorption of a photon is detected from the loss of energy [39]. There are two types of scattering that can occur: elastic and inelastic [39]. Elastic scattering occurs when the scattered photon has the same energy as the incident photon, this type of scattering is commonly referred to as Rayleigh scattering **(**Figure 3) [39]. Inelastic scattering occurs when the photon excites the molecule into an unstable virtual state for a brief time before inelastically scattering from

the molecule, this is Raman scattering (Figure 3) [39]. There are two types of inelastic scattering that can occur: Stokes and anti-Stokes, seen in Figure 3 [39]**.** Stokes scattering occurs when the absorbed photon has a higher energy than the emitted photon after interaction with matter (Figure 3) [39]. In contrast, anti-Stokes scattering occurs when the absorbed photon has lower energy than the emitted photon after interaction with matter (Figure 3) [39].

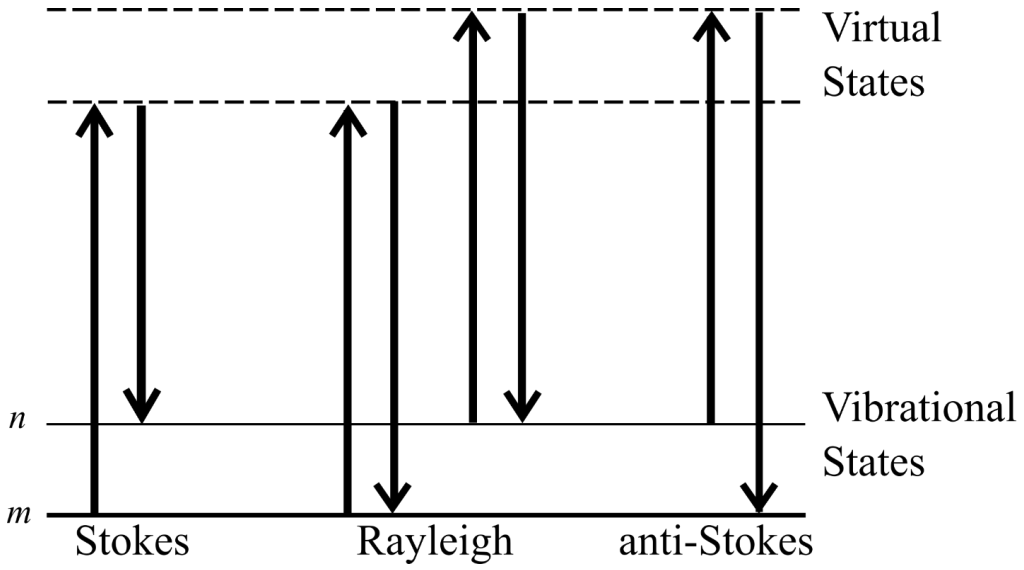

Figure 3. Diagram of Rayleigh and Raman scattering, shown for the ground state *m* and the excited state *n*.

Compared to elastic, or Rayleigh scattering, Raman scattering is a relatively weak process where one in every 10^6 - 10^8 photons scatter inelastically [39]. Raman spectroscopy uses the scale of wavenumbers $\bar{\upsilon}$ (cm^{-1}), which are derived as [38,39]:

$$\lambda = \frac{c}{\upsilon} \tag{5}$$

$$\upsilon = \frac{\Delta E}{h} \tag{6}$$

$$\bar{\upsilon} = \frac{\upsilon}{c} = \frac{1}{\lambda} \quad (7)$$

Where λ is the wavelength, c is the speed of light, E is energy, υ is frequency, and h is Planck's constant [38,39].

Raman Spectroscopy on Glasses

When looking at an amorphous material, such as glass, with no long-range order, the peaks observed in a Raman spectrum are not sharp and as well-defined as their crystalline counterparts [42]. The Raman spectra of amorphous materials presents as broad, Gaussian shaped peaks. For silicate glasses, these vibrational modes have been thoroughly investigated and studied [43–45]. As seen in Figure 4, the Raman spectrum of the crystalline, α-quartz (space group #154, $P3_221$) [46] sample shows narrow, sharp peaks while the amorphous fused quartz sample has broad peaks in the Raman spectrum. While both the α-quartz and fused quartz are made of the same compounds: silicon and oxygen, the way that they are bonded leads to stark differences in the Raman spectrum.

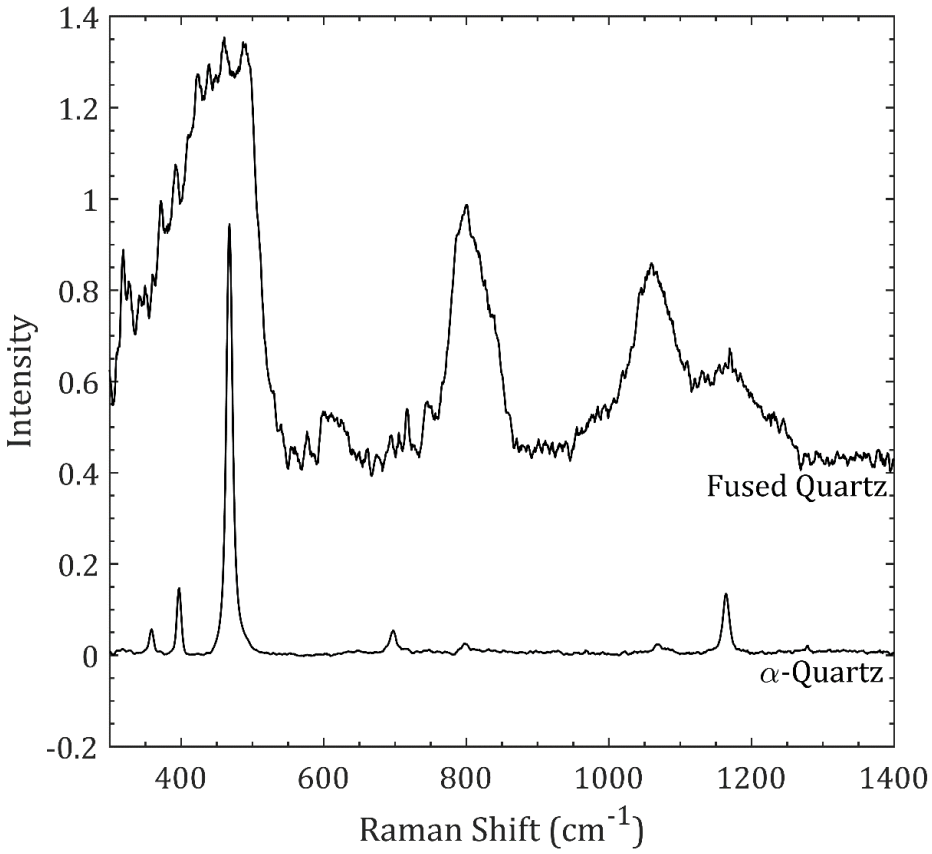

Figure 4. Raman spectra of fused quartz (top) and α-quartz (bottom).

EXPERIMENTAL MEASUREMENT TECHNIQUES

Samples

Borosilicate Glass Samples

Three borosilicate glass samples with varying B_2O_3 content were investigated in this study. The sample compositions are seen in Table 1. The commercially available Borofloat sample was reprocessed at U.S. Army Research Laboratory using the furnace conditions in Table 2. The commercial Borofloat was first crushed and then heat cycled: starting at 5.25°C and is heated to 1540°C and held for 17 hours. Then dropped to 0.9°C and then the temperature was raised to 1090°C and held for 4.5 hours, and the heating/cooling cycle continues, as described in *Table 2*. The commercial Borofloat sample was reprocessed in the same manner as the Low and High B samples to ensure sample uniformity since the exact processing details for the commercial Borofloat are unknown.

Table 1. Borosilicate glass sample compositions determined via inductively coupled plasma atomic emission spectroscopy by U.S. Army Research Laboratory.

Compound	Borofloat	Low B	High B
Al_2O_3	2.4	2.06	2.1
B_2O_3	12.45	8.46	17.57
BaO	0	0.17	0.04
CaO	0.02	0.04	0.04
Fe_2O_3	0.01	0.02	0.02
K_2O	0.57	0.42	0.41
Na_2O	3.4	3.37	3.34
SiO_2	81.1	85.41	76.43
TiO_2	0	0.01	0.01
ZrO_2	0.03	0.01	0.01

Table 2. Reprocessing Furnace Cycle Details for SCHOTT BOROFLOAT ® 33 Glass done by U.S. Army Research Laboratory.

Starting Temperature (°C)	Ending Temperature (°C)	Time* (hours)
5.25	1540	17
0.9	1090	4.5
0.7	935	3.5
0.5	820	3.5
0.3	590	14
0.2	535	8.5
0.2	450	5.5
0.2	25	End

*Time held at each ending temperature (°C)

Bulk Metallic Glass Sample

The Zr-based bulk metallic glass sample investigated in this dissertation is the commercially available Vit 106a ($Zr_{58.5}Cu_{15.6}Ni_{12.8}Al_{10.3}Nb_{2.8}$) from Materion.

Beamline 16-BM-B Overview

The multi-angle energy-dispersive X-ray diffraction (EDXD) and white-beam radiography research discussed in this thesis was conducted at Beamline 16-BM-B, The Advanced Photon Source, Argonne National Laboratory.

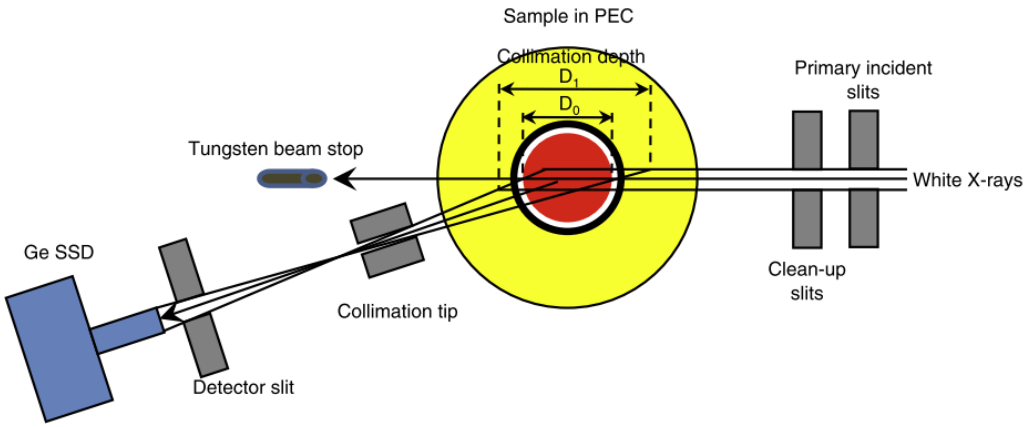

Figure 5. A Schematic of the energy-dispersive X-ray diffraction setup at Beamline 16-BM-B [33].

From "Toward comprehensive studies of liquids at high pressures and high temperatures: Combined structure, elastic wave velocity, and viscosity measurements in the Paris–Edinburgh cell" by Y. Kono, C. Park, C. Kenney-Benson, G. Shen, and Y. Wang, 2014, Physics of the Earth and Planetary Interiors, 228, p. 272. Copyright 2014 by Elsevier B.V. Reprinted with permission.

Located 25 m from the white X-ray source are the primary incident slits (Figure 5), which determine the size of the X-ray beam onto the sample [33]. The secondary, clean-up slits, seen in Figure 5, are constantly held at a 10% larger slit size as compared to the primary incident slits to clean up scatter before the white X-ray beam hits the sample [33]. After the beam reaches the sample in the Paris-Edinburgh (PE) press, the diffracted beam then passes through the collimation tip, located 60 mm from the center of the sample (Figure 5) [33]. Once collimated, the diffracted beam passes through the detector slit and is collected by the Germanium solid-state detector (Ge-SSD) (Figure 5) [33].

High-Pressure Paris-Edinburgh Press Cell Assembly

The borosilicate glass samples were quasi-hydrostatically in a PE cell at ambient temperature.

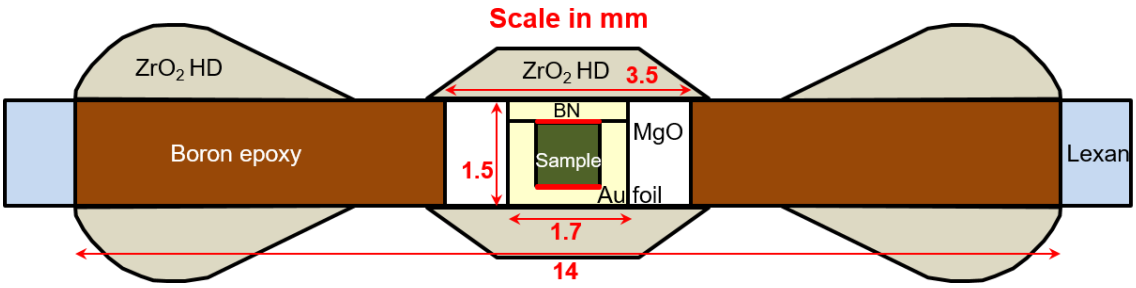

Figure 6. A schematic illustration of the sample assembly utilized in the PE press [47].

From "White-beam X-ray diffraction and radiography studies on high-boron-containing borosilicate glass at high pressures" by K. J. Ham, Y. K. Vohra, Y. Kono, A. A. Wereszczak, and P. Patel, 2017, High Pressure Research, 37, p. 235. Copyright 2017 by Informa UK Limited, trading as Taylor & Francis Group. Reprinted with permission.

The sample chamber used in this experiment consists of a cylindrical borosilicate glass sample (height 0.7 mm, diameter 1 mm), housed in a hexagonal boron nitride (h-BN) cup with an h-BN cap (Figure 6). This sample assembly is enclosed in a magnesium oxide (MgO) ring, which sits in a boron epoxy disk, with sintered high-density ZrO_2 supports, all enclosed in a supportive Lexan ring. Gold foil (2 μm thick) was placed on both the top and bottom of the glass sample and used as the pressure standard as well as the uniaxial compression fiducial markers in the radiography experiments. A photograph of the sample assembly loaded onto the bottom PE anvil is shown in Figure 7 with a 14 mm scale bar.

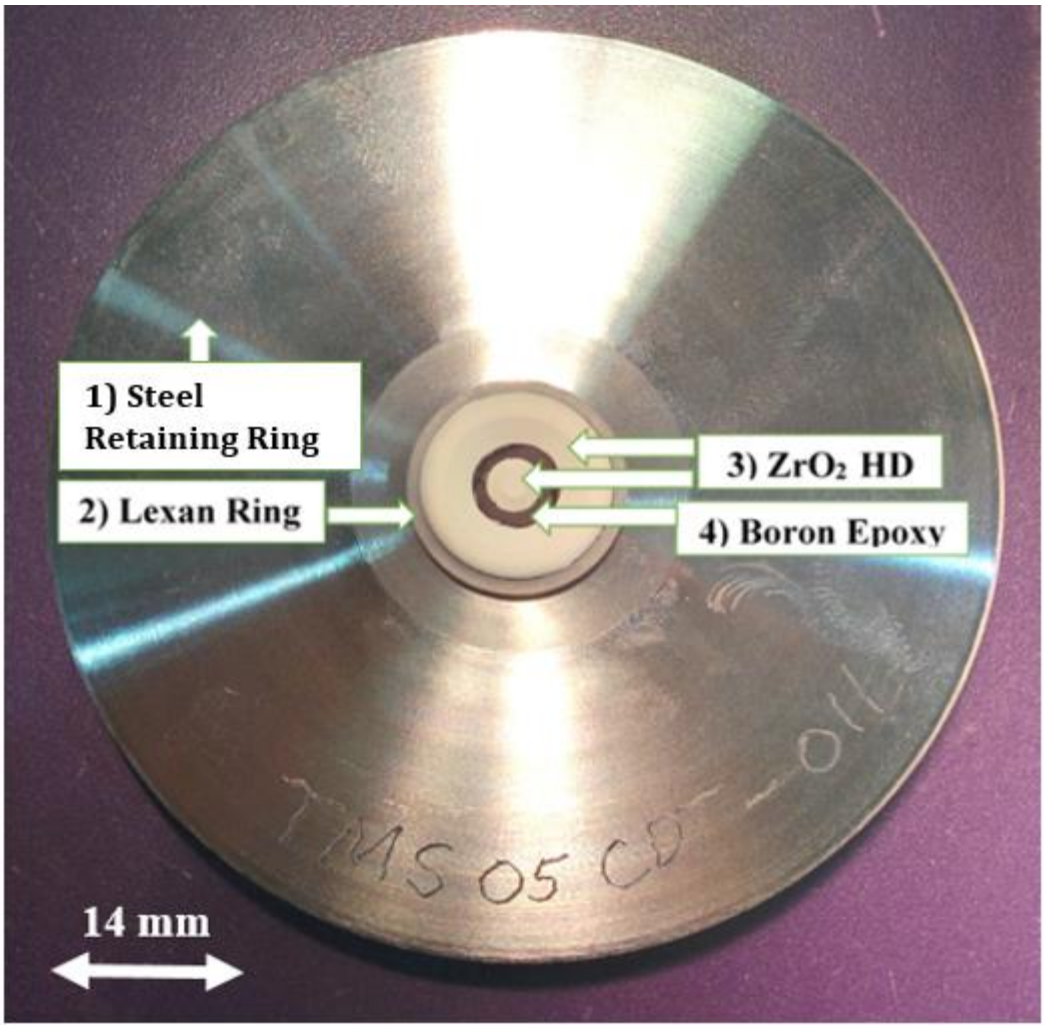

Figure 7. A photograph of the bottom PE anvil and cell assembly.

High-Pressure, High-Temperature Paris-Edinburgh Press Cell Assembly

White-beam energy-dispersive X-ray diffraction and radiography were conducted on a sample of Materion's Vit 106a, $Zr_{58.5}Cu_{15.6}Ni_{12.8}Al_{10.3}Nb_{2.8}$ (at%) under high-pressure and high-temperature conditions. The cell assembly used in the PE press is shown in Figure 8. Each BMG sample (green square in Figure 8) is cut, using a diamond saw, into 0.5 mm X 0.5 mm X 0.2 mm foils, then loaded into a cylindrical BN capsule with two pBN pins on either side, holding the sample in place [33]. A graphite heater sleeve is then slid around

the BN cylinder (Figure 8). A MgO ring is placed between the graphite heater and the Boron Epoxy ring to increase the stability of the cell assembly, in addition to being used as the pressure standard (Figure 8) [33]. The boron epoxy gasket and the ZrO_2 caps are included in the assembly to provide thermal insulation for high-temperature experiments, and the Lexan (polycarbonate plastic) ring is used to stabilize the assembly (Figure 8) [33]. The Mo foil, Ta rod, and Ta foil are all used to conduct current through the graphite heater in order to heat the sample (Figure 8) [33].

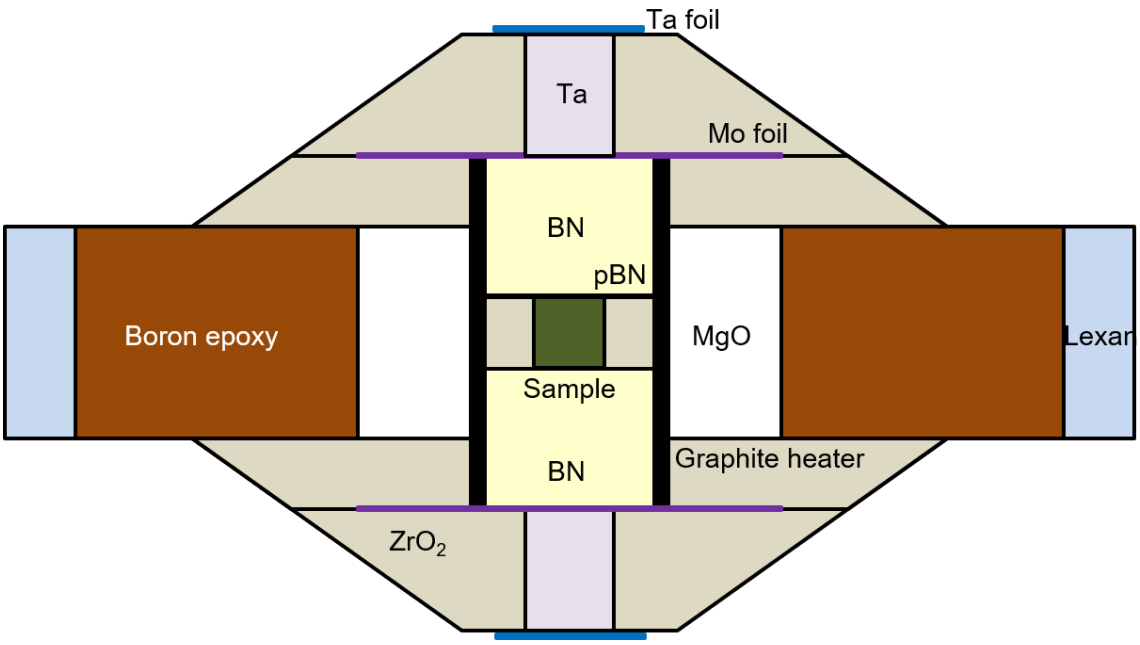

Figure 8. A schematic of the sample holder used in the PE press for resistive heating.

Pressure and Temperature Determination

The gold foil (Space group: $Fm\bar{3}m$, No. 225) placed on the top and bottom of the cylindrical glass sample was used as the metallic pressure standard [34].

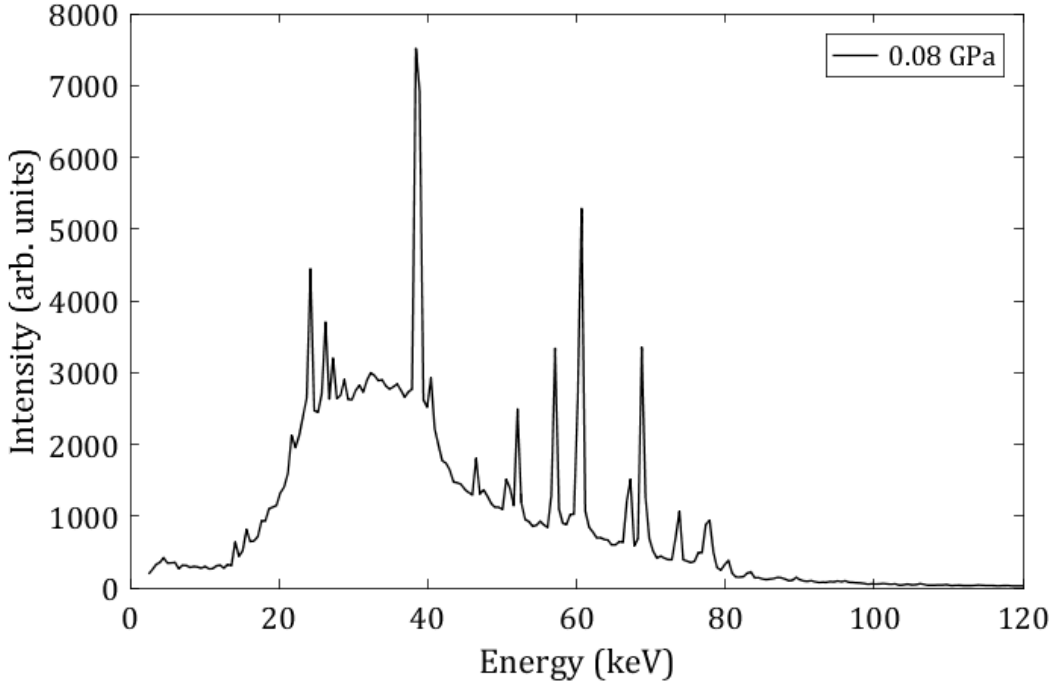

Figure 9. Raw EDXD spectrum for gold foil at 0.08 GPa.

The raw EDXD spectrum (Figure 9), as a function of energy (keV), was converted into a spectrum in terms of d-spacing (Å) (Figure 10) using Bragg's Law and photon energy. The lattice parameter *a* for a cubic Au crystalline structure was found from a fit to the positions of the (311), (222), (400), (331), (420), (422), (511), (531), (620), (622) peaks in the converted EDXD spectra of gold (Figure 10), recorded at a scattering angle of $2\theta = 15°$.

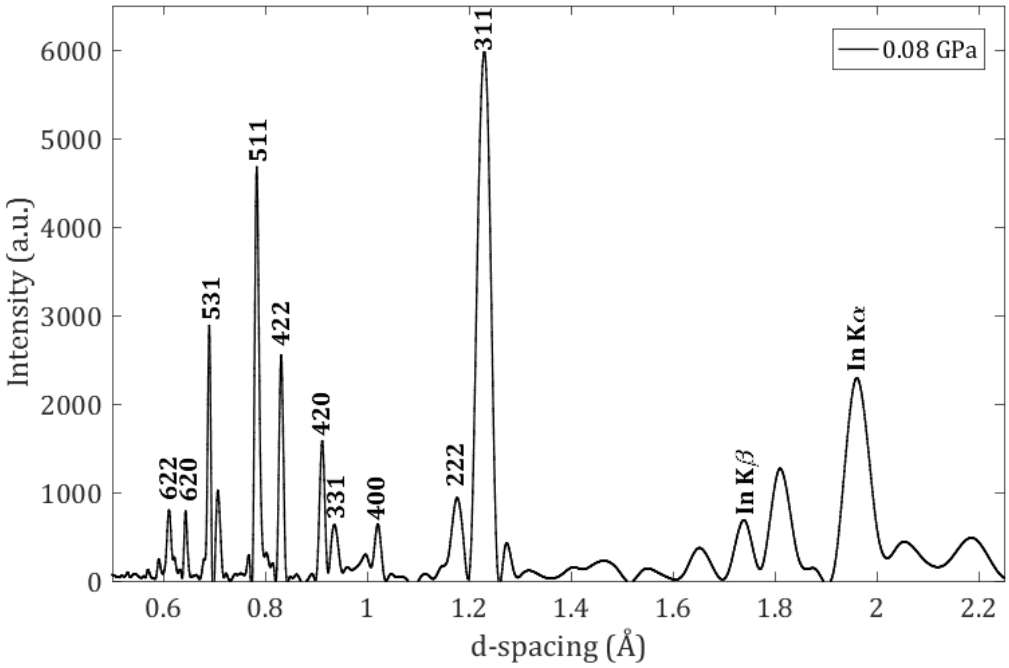

Figure 10. Background subtracted gold foil spectrum at 0.08 GPa with Miller indices labeled.

The bulk modulus B_0 = 165.8 GPa (where $B_0 = \frac{E}{3(1-2\nu)}$ and E is the elastic modulus and ν is Poisson's ratio), the first derivative of the bulk modulus B_0' = 5.14, and the initial volume V_0 = 67.850 Å^3 at ambient pressure and temperature were used with the cell volume V to calculate the sample's static pressure using the third-order Birch-Murnaghan equation of state (Eqn. 8) [34,35].

$$P = \frac{3}{2}B_0\left[\left(\frac{V_0}{V}\right)^{\frac{7}{3}} - \left(\frac{V_0}{V}\right)^{\frac{5}{3}}\right]\left\{1 + \frac{3}{4}(B_0' - 4)\left[\left(\frac{V_0}{V}\right)^{\frac{2}{3}} - 1\right]\right\} \quad (8)$$

For the BMG crystallization studies, MgO (space group #225, $Fm\bar{3}m$) was used as the pressure standard [48,49]. The bulk modulus, B_0 = 160.9 GPa, the first derivative of the bulk modulus, B_0' = 4.35(10), and the initial sample volume, V_0 = 74.71 Å^3 were used

to calculate the high-pressure, high-temperature sample pressure using the third-order Birch Murnaghan equation of state (Eqn. 8) [49].

$$\Delta P_{th}(V,T) = \left(\frac{\gamma}{V}\right)\Delta E_{th} \quad (9)$$

$$\Delta E_{th} = E_{th}(V,T) - E_{th}(V,T_0) \quad (10)$$

$$E_{th} = 9nN_A k_b T\left(\frac{\theta}{T}\right)^{-3}\int_0^{\theta/T}\frac{x^3}{e^x-1}dx \quad (11)$$

Where $\gamma = 1.53$ is the Grüneisen parameter, $\theta = 773\ K$ is the Debye temperature, n is the number of atoms in the formula unit ($n = 2$), N_A is Avogadro's number (6.022 x 10^{-23} J K^{-1}), and k_b is Boltzmann's constant (1.381 x 10^{-23} J K^{-1}) [49].

For the high-temperature portion of the experiment, the sample temperature is calculated using Equation 12, where set power and oil pressure are inputted, and the sample temperature is calculated. This equation's parameters, seen in Table 3 were determined using a fit to experimental data, where the temperature was known from a thermocouple placed in the center of the PE cell assembly in lieu of a sample.

$$W = K_0 + K_1T + K_2P + K_3T^2 + K_4TP + K_5P^2 + K_6T^3 + K_7T^2P + K_8TP^2 \quad (12)$$

Where W is power in Watts, T is temperature in °C, P is oil pressure in psi, and $\sum_{i=0}^{8} K_i$ are fit coefficients. The fitted coefficients are seen in Table 3.

Table 3. Parameters used in power, temperature, and oil pressure relation.

Parameter	Value
K_0	0
K_1	0.24448
K_2	-0.00146
K_3	-3.23E-05
K_4	1.59E-05
K_5	4.91E-08
K_6	1.02E-08
K_7	-3.06E-09
K_8	-3.21E-10

White-Beam Radiography

The method to determine sample volume from radiography images is described. The raw radiography image of the sample is cropped and rotated so that line scans can be performed on the vertical and horizontal extents of the sample area. Each radiograph is cropped to a 651 px X 701 px image for easier analysis since there is no need to include the rest of the sample assembly to obtain the sample dimensions. The darker area seen in Figure 11 A is the sample and the lighter surrounding area is the h-BN capsule. The sample area is darker since it is a higher-Z material as compared to the h-BN. The black line shown in Figure 11 A at y = 300 px is used as an example of how the analysis is conducted. Figure 11 B shows the brightness for each pixel along the line profile at y = 300 px. The sharp peaks correspond to statistical noise which shows up in the radiograph, and a smoothing curve is applied to the data to remove them. Figure 11 C shows the first derivative d(Brightness)/d(Pixel) for the line profile at y = 300 px. In this figure, a Gaussian fit

(Equation 13) is applied to the data set to obtain the two edges in the sample for the line profile at y = 300 px.

$$y(x) = a_1 e^{-\left(\frac{x-b_1}{c_1}\right)^2} + a_2 e^{-\left(\frac{x-b_2}{c_2}\right)^2} \quad (13)$$

Where a_1 is the height of the first peak, a_2 is the height of the second peak, b_1 is the position of the center of the first peak, b_2 is the position of the center of the second peak, c_1 is the Gaussian RMS width of the first peak, c_2 is the Gaussian RMS width of the second peak, and x is

This figure only shows the fit for a one-line profile in one direction. To obtain the sample volume this same method has been applied to 300 channels in both the x and y-direction (200 px – 500 px). Since this is a foil with thickness the assumption that the thickness is changing with pressure at the same rate that the two seen dimensions are changing is applied. With this assumption, the thickness of the sample is:

$$Side\ 3 = \frac{Side\ 1 + Side\ 2}{2} \quad (14)$$

The volume of the sample is calculated as:

$$Volume = Side\ 1 * Side\ 2 * Side\ 3 \quad (15)$$

The sample volumes are then normalized by the initial ambient sample volume.

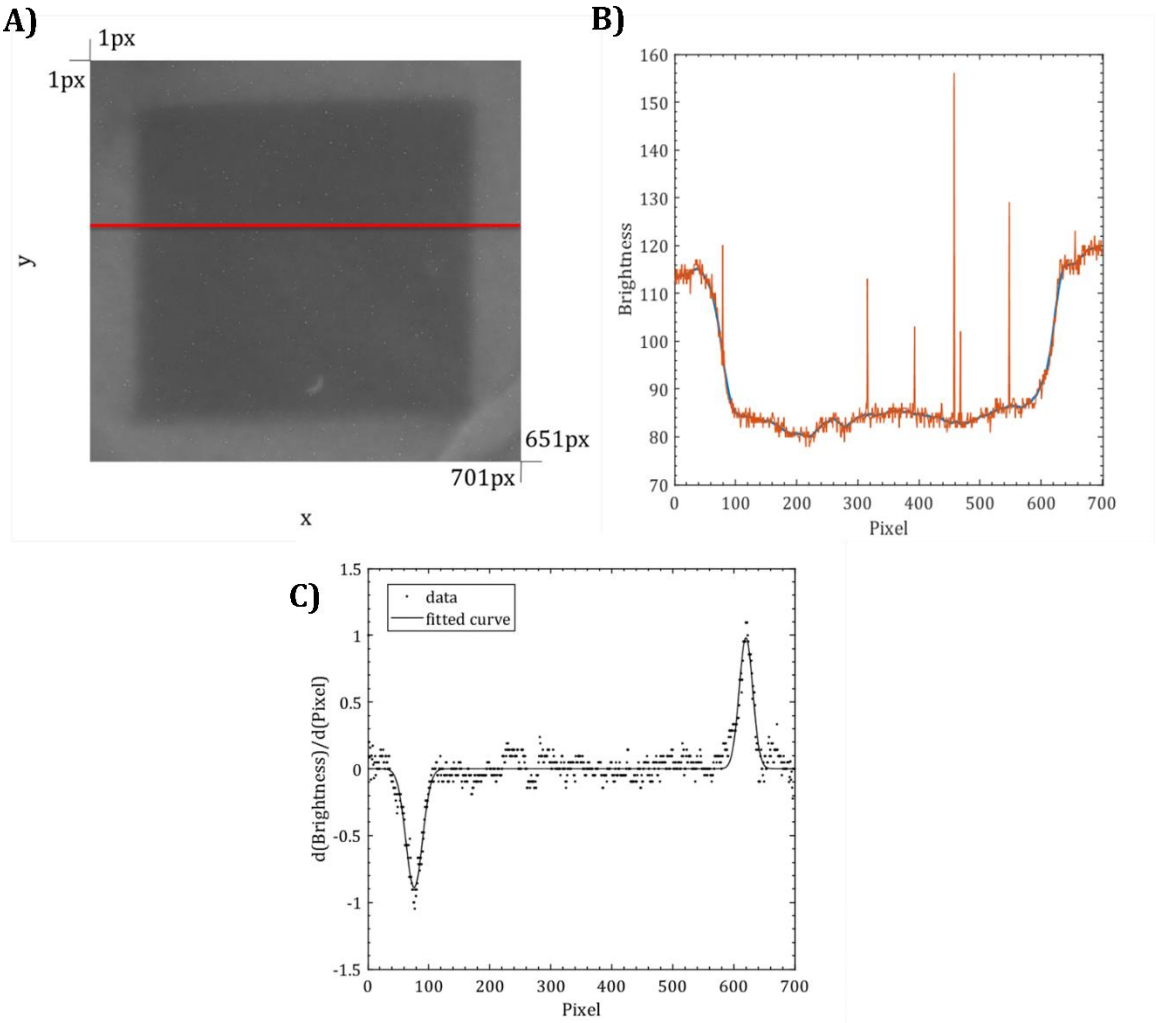

Figure 11. A) Radiography image of Vit106a sample at ambient conditions. Darker area is the sample, the lighter area is the surrounding h-BN; the line is shown at y = 300 px indicates the line scan shown in B. B) The smoothed brightness line scan at y = 300px. C) d(Brightness)/d(Pixel) at y = 300 px; the two Gaussian peaks indicate the position of the edges for the sample.

Raman Spectroscopy

Raman spectroscopy was conducted on a bulk glass sample and the recovered sample (from multi-angle EDXD experiments) at ambient conditions at University of Alabama at Birmingham. A grating with 1200 groves/mm and a lens with 25× magnification were used in this experiment. A 300 mW laser (λ=532 nm) was used, and

imaging was performed with a liquid nitrogen cooled Princeton Instruments PI ACTION charge-coupled device (CCD) detector. An argon gas lamp was used to calibrate the Raman spectrometer, centered at 780 cm^{-1}. For the borosilicate glass samples, a 600-second exposure time and 3 accumulations were the experimental settings used to obtain each spectrum.

Flotation Density Measurements

Floatation density measurements were conducted on borosilicate glass samples before and after compression to high pressures with a Paris-Edinburgh Press. High specific gravity fluid, lithium metatungstate with a density of 2.950 gm/cc, was used for the following density measurements. P-10 (0.5 - 10.0 μL) and P-1000 (0.1 – 1.0 mL) micropipettes were used to add deionized water to the lithium metatungstate to change the density of the liquid.

Figure 12. Density test for the 12.45% B_2O_3 borosilicate glass sample on the magnetic stir plate. The sample is shown suspended in the liquid in the red circle.

BOROSILICATE GLASS STUDIES

Energy-Dispersive X-Ray Diffraction

EDXD was conducted to look at the behavior of the various atomic pairs as the sample went to pressure. The various peak positions in the *G(r)* spectrum correspond to internuclear distances between various atomic species within the sample. The High B sample's G(r) was plotted in Figure 13.

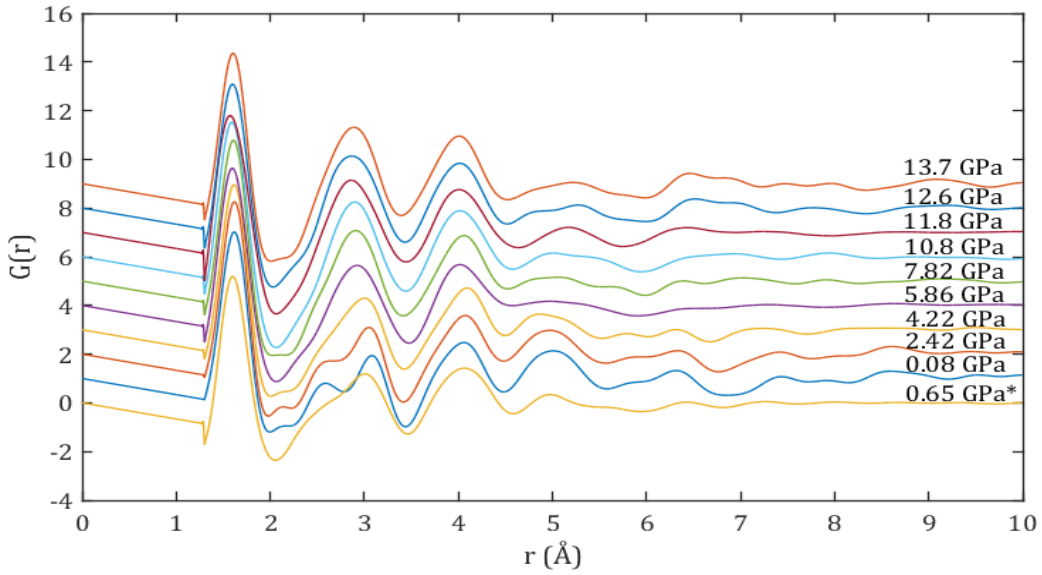

Figure 13. The reduced pair distribution function G(r) for the sample of high-boron containing a sample of borosilicate glass. The '*' denotes the decompression spectrum [47].

The first peak in the reduced pair distribution function *G(r)* (Figure 13) appears around 1.6 Å, which corresponds to the internuclear distance r_{Si-O} of nearest neighbor Si–O bonds, which is shown as the internuclear distance between the atoms labeled $Si_{[1]}$ and

$O_{[1]}$ in Figure 12(a). The shape of the first peak in the *G(r)* spectrum remains consistent up to pressures of 13.7 GPa (Figure 13). The value 1.606 ± 0.001 Å obtained for 17.6% boron-containing borosilicate glass at ambient conditions closely corresponds to values from other studies of borosilicate glasses [33,50–52].

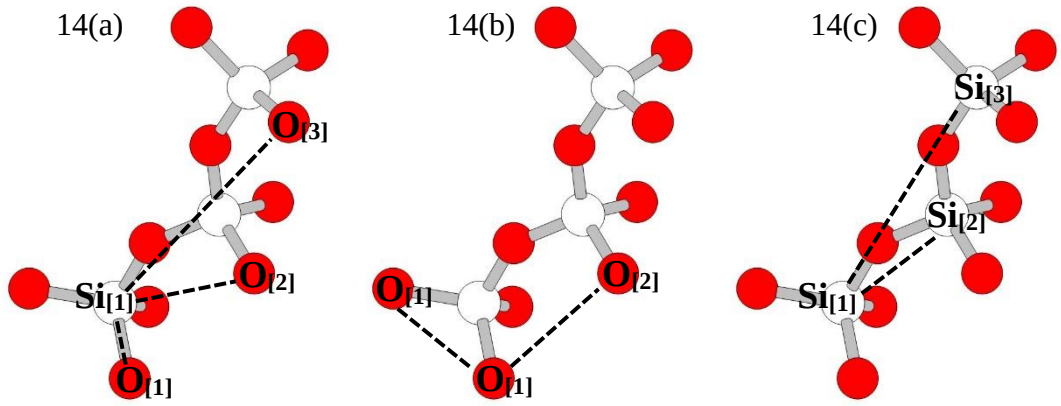

Figure 14. (a) A representation of the bonding of first nearest neighbor Si-O bonds (Si[1]-O[1]) and the second nearest neighbor Si-O bonds (Si[1]-O[2]), (b) A representation of the bonding of first nearest neighbor O-O bonds (O[1]-O[1]), and (c) A representation of (Si[1]-Si[2]).

Under compression, the Si–O bond length shortens overall (Fig. 13(a)) but returns to approximately the same starting bond length upon decompression to ambient conditions. In the initial ambient *G(r)* spectrum at 0.08 GPa, there are two distinct peaks centered at 2.598 ± 0.001 and 3.079 ± 0.0005 Å which correspond to nearest neighbor O–O from the SiO_2 network (Figure 14(b)) and nearest neighbor Si–Si (Figure 14(c)) distances, respectively. These nearest neighbor distances are in good agreement with the O–O and Si–Si internuclear distances determined for borosilicate glass samples from various studies [50–52]. As the static sample pressure is increased, the two peaks become less distinct and at 4.22 GPa the Si-Si peak absorbs the O–O peak as a shoulder, and at 7.82 GPa the O–O shoulder is completely absorbed by the Si-Si peak (Figure 15(b)). From

ambient pressure to 5.86 GPa the O–O bond length has a consistent trend of decreasing bond length. After decompression to ambient conditions, the observed internuclear distance of O–O is slightly shorter as compared to the initial ambient internuclear distance (Figure 15(b)).

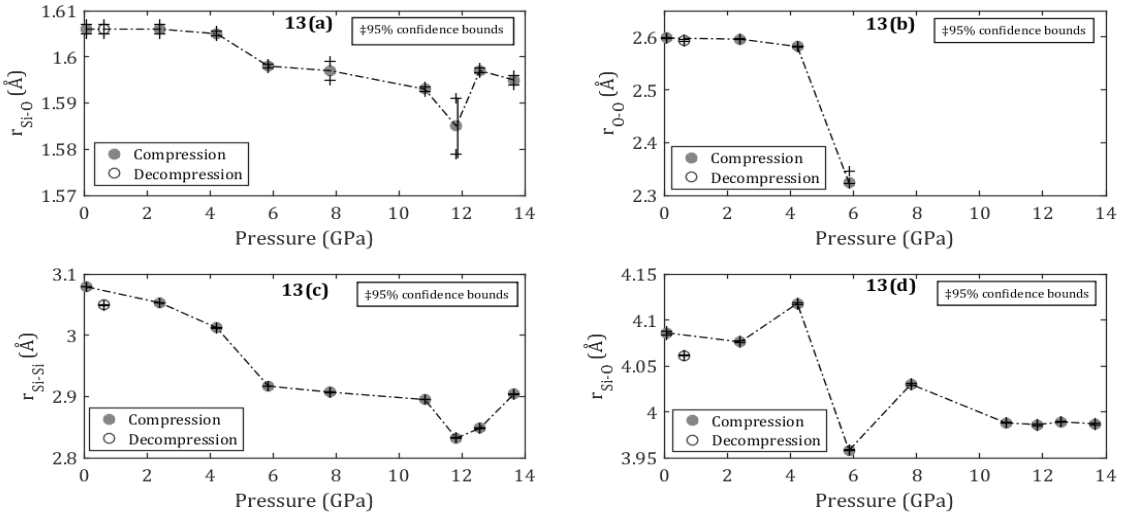

Figure 15. The peak positions obtained from G(r) for (a) nearest neighbor Si-O, (b) nearest neighbor O-O, (c) nearest neighbor Si-Si, and (d) second nearest neighbor Si-O [47].

The nearest neighbor Si–Si peak has a consistently decreasing internuclear distance until 11.8 GPa where it shows an increasing trend until the end of compression (Figure 15(c)) The Si–O second nearest neighbor internuclear distance change with pressure is shown in Figure 15(d) where it shows a sharp decrease from 4.22 to 5.86 GPa and a small increase and general leveling off after 5.86 GPa. The compression effect seen in Figure 15(d) is an indication of a permanent deformation after decompression. The reduced pair distribution

function G(r) obtained on decompression is qualitatively like ambient pressure function (Fig. 11); however, the doublet representing O–O and Si –Si distances is broadened, and the doublet is less distinct. All the internuclear distances at various pressures are summarized in Table 4.

Table 4. Bond distances in 17.6% boron-containing borosilicate glass at various pressures obtained from reduced pair distribution function G(r). The decompression pressure is marked with an '*.'

Pressure (GPa)	r_1 (Å)	r_2 (Å)	r_3 (Å)	r_4 (Å)
0.08	1.606 ± 0.001	2.597 ± 0.001	3.079 ± 0.0005	4.084 ± 0.002
2.42	1.606 ± 0.001	2.595 ± 0.001	3.053 ± 0.0005	4.076 ± 0.001
4.22	1.605 ± 0.0005	2.581 ± 0.001	3.011 ± 0.001	4.118 ± 0.001
5.86	1.598 ± 0.0005	2.323 ± 0.001	2.917 ± 0.0005	3.958 ± 0.0005
7.82	1.595 ± 0.002	-	2.907 ± 0.0005	4.03 ± 0.001
10.8	1.593 ± 0.0005	-	2.895 ± 0.0005	3.988 ± 0.0005
11.8	1.579 ± .006	-	2.832 ± 0.0005	3.986 ± 0.001
12.6	2.597 ± 0.0005	-	2.848 ± 0.001	3.689 ± 0.0005
13.7	1.594 ± 0.001	-	2.904 ± 0.001	3.986 ± 0.001
0.6	1.606 ± 0.001	2.594 ± 0.002	3.049 ± 0.0005	4.061 ± 0.0005

From "White-beam X-ray diffraction and radiography studies on high-boron-containing borosilicate glass at high pressures" by K. J. Ham, Y. K. Vohra, Y. Kono, A. A. Wereszczak, and P. Patel, 2017, High Pressure Research, 37, p. 240. Copyright 2017 by Informa UK Limited, trading as Taylor & Francis Group. Reprinted with permission.

White-Beam Radiography

α-Fe Radiography Validation

A validation of method was conducted on a sample of α-Fe (space group: $Im\bar{3}m$, No. 229, lattice parameter: a = 2.8664 Å [55]) to prove radiography a reliable method to determine bulk volume measurements for determination of the equation of state for amorphous materials. The sample pressure was determined from the diffraction of the gold

foil (space group: $Fm\bar{3}m$, No. 225) surrounding the α-Fe sample. The cylindrical α-Fe sample was compressed to 6.3 GPa in a PE press and then decompressed to ambient pressure. The radiography images of the sample are seen in Figure *16* where the decompression radiograph is seen denoted with an '*.' The sample height was measured from the top to bottom gold foil and the sample width was found from the left to right gold foil in pixels and converted using the conversion: $\frac{0.850\ \mu m}{1\ pixel}$.

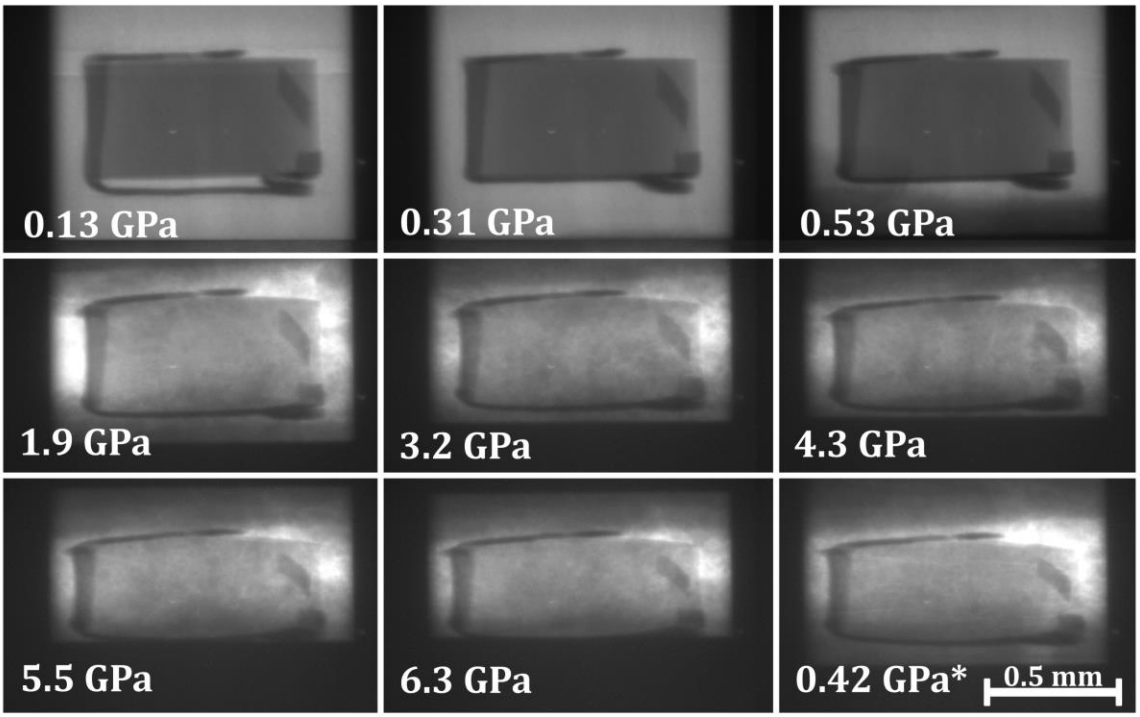

Figure 16. Radiography images for α-Fe.

From "Pressure Induced Densification and Compression in a Reprocessed Borosilicate Glass" by Kathryn J. Ham, Yoshio Kono, Parimal J. Patel, Steven M. Kilczewski, and Yogesh K. Vohra, 2018, Materials, 11(1), p. 114. Copyright 2018 by the authors. Reprinted with permission.

The initial ambient height, H_0 and initial ambient width, W_0 were used to normalize the sample height, H and sample width, W so that at 0.13 GPa the sample height, $H/H_0 = 1$

and the sample width, $W/W_0 = 1$, with experimental values seen in Table 5. The $(V/V_0)^*$ values in Table 5 are determined from the EDXD spectra of α-Fe seen in Figure 17.

Table 5. H/H_0, W/W_0, V/V_0 and $(V/V_0)^*$ for α-Fe obtained from radiography images. These values were normalized by the initial ambient value.

Pressure (GPa)	$\frac{H}{H_0}$	$\frac{W}{W_0}$	$\left(\frac{V}{V_0}\right)$	$\left(\frac{V}{V_0}\right)^*$
0.13 ± 0.18	1.0000 ±	1.0000 ±	1.0000 ±	1.0000 ±
0.31 ± 0.21	0.9967 ±	1.0008 ±	0.9984 ±	0.9987 ±
0.53 ± 0.28	0.9900 ±	1.0034 ±	0.9967 ±	0.9964 ±
1.93 ± 0.20	0.9685 ±	1.0110 ±	0.9898 ±	0.9900 ±
3.19 ± 0.28	0.9254 ±	1.0295 ±	0.9807 ±	0.9814 ±
4.33 ± 0.30	0.8905 ±	1.0472 ±	0.9766 ±	0.9757 ±
5.52 ± 0.28	0.8557 ±	1.0649 ±	0.9703 ±	0.9693 ±
6.29 ± 0.33	0.8425 ±	1.0708 ±	0.9659 ±	0.9656 ±

The $(V/V_0)^*$ was obtained from X-ray diffraction measurements

The $(V/V_0)^*$ was obtained from X-ray diffraction measurements (Figure 17). In Table 5, the error bars for the pressure (GPa) were determined as the standard deviation of the pressure, determined by the third-order Birch-Murnaghan equation of state for each lattice parameter.

Energy-dispersive X-ray diffraction was taken for α-Fe at each incremental pressure step and the spectra with labeled Miller indices (HKLs) are seen in Figure 17. The high-pressure volumes obtained from EDXD of α-Fe were normalized by the initial ambient pressure volume, and are seen in Table 5 (denoted with an '*'), Figure 18 (denoted as '◊').

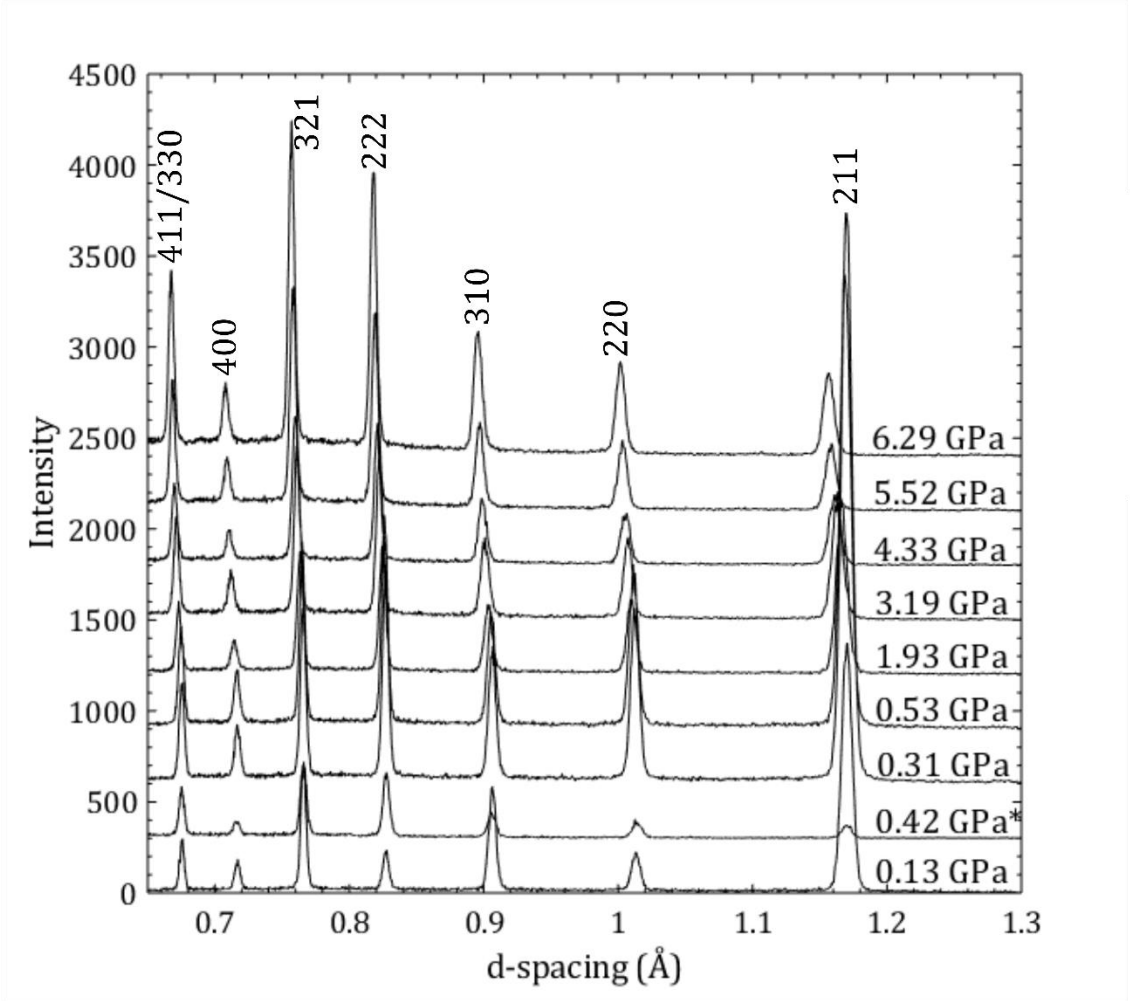

Figure 17. Energy-dispersive X-ray diffraction of the α-Fe sample. The '*' indicates the decompression ambient spectrum at 0.42 GPa.

After the radiography and EDXD sample volumes were obtained for α-Fe, the bulk modulus, B_0 was calculated for the volumes obtained by each method and compared to literature values determined from ultrasonic methods [56]. Guinan *et. al.* determined a bulk modulus of 166.4 ± 1.7 GPa and a $B_0' = 5.29$ [56]. A constraint was placed on the nonlinear least squares fit to determine the bulk modulus of α-Fe by radiography and EDXD measurements, where B_0' was held constant at 5.29 in order to better compare the bulk

modulus's obtained between the three methods. The third-order Birch-Murnaghan equation of state was used where the sample pressure, P was previously determined from gold foil, the sample volume, V was determined separately from radiography and EDXD measurements of α-Fe, B_0' was fixed at 5.29, and B_0 was fit with a nonlinear least squares fit, which converged with an R^2 value of 0.997 for the white-beam radiography measurements with B_0 = 167.6 ± 5.3 GPa, and an R^2 value of 0.9978 for the energy-dispersive X-ray diffraction measurements with B_0 = 164.4 ± 4.4 GPa.

$$P = \frac{3}{2}B_0\left[\left(\frac{V_0}{V}\right)^{\frac{7}{3}} - \left(\frac{V_0}{V}\right)^{\frac{5}{3}}\right]\left\{1 + \frac{3}{4}(B_0' - 4)\left[\left(\frac{V_0}{V}\right)^{\frac{2}{3}} - 1\right]\right\}$$

The third-order Birch Murnaghan equation of state (EOS) fits are seen in Figure 18 where the experimentally determined $(\frac{V}{V_0})$ from radiography measurements are seen as '○,' the experimentally determined $(\frac{V}{V_0})$ from energy-dispersive X-ray diffraction measurements are seen as '◊,' the EOS fit for the radiography measurements is seen as a solid line '—,' the EOS fit for the EDXD measurements is seen as a dashed line '----,' and the EOS fit from Guinan *et. al.* [56] is seen as a dotted line '·····.'

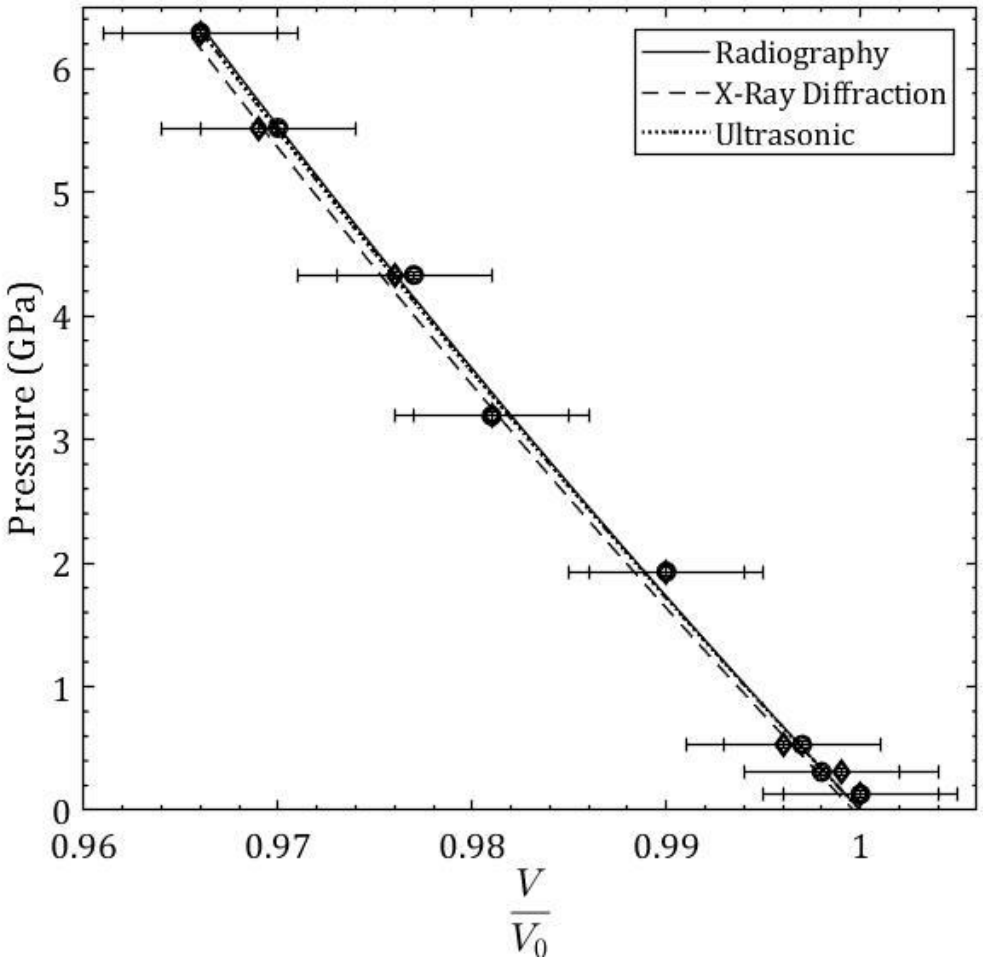

Figure 18. The third-order Birch-Murnaghan equation of state fit for α-Fe, using radiography data (○), energy-dispersive X-ray diffraction data (◊), and reference EOS fit (ultrasonic methods).

From "Pressure Induced Densification and Compression in a Reprocessed Borosilicate Glass" by Kathryn J. Ham, Yoshio Kono, Parimal J. Patel, Steven M. Kilczewski, and Yogesh K. Vohra, 2018, Materials, 11(1), p. 114. Copyright 2018 by the authors. Reprinted with permission.

A summary of the bulk modulus values determined from the radiography and EDXD methods are seen in Table 6. The percent difference, defined as:

$$\frac{|V_E - V_R|}{\left[\frac{V_E + V_R}{2}\right]} \times 100$$

Where V_E is the experimentally obtained value and V_R is the reference value, can be calculated for the radiography and EDXD B_0 values. The bulk modulus value obtained from radiography methods has a percent difference of 0.7%, as compared to the reference value from ultrasonic measurements [56]. The bulk modulus value obtained from EDXD methods has a percent difference of 1.2%, as compared to the reference value from ultrasonic measurements [56]. Overall, the percent difference between both experimentally obtained bulk modulus values is small ~1%, which leads to the conclusion that white-beam radiography is a valid method to determine the bulk modulus of samples.

Table 6. Bulk modulus values for α-Fe determined from radiography, EDXD, and ultrasonic methods [56].

	Radiography	**EDXD**	**Guinan *et. al.*** [56]
B_0	167.6 ± 5.3 GPa	164.4 ± 4.4 GPa	166.4 ± 1.7 GPa
B_0'	5.29	5.29	5.29
% difference	0.7%	1.2%	-

Reprocessed Borofloat Sample

White-beam radiography was conducted on a sample of reprocessed borosilicate glass. Since borosilicate glass is a low-Z material, the contrast between the sample and the sample holder is small. Gold foil is placed along the top, bottom, and sides of the cylindrical sample so that the extents of the sample can be seen in the radiographs (Figure 19).

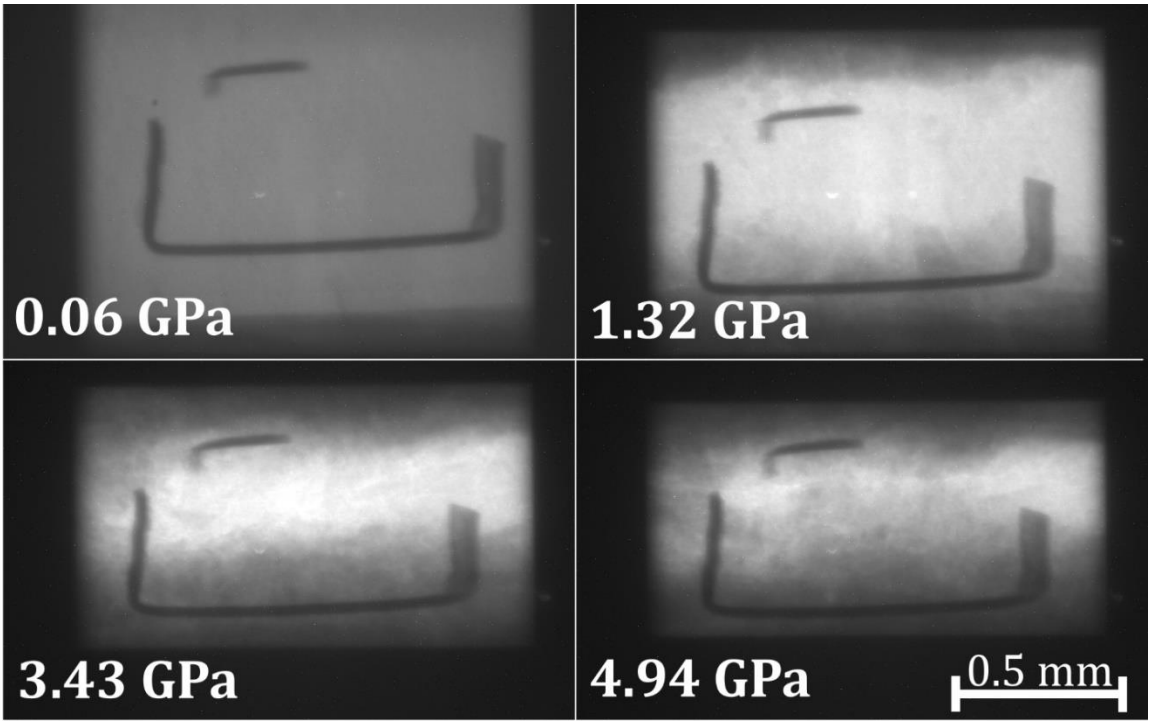

Figure 19. X-ray Radiography images of the reprocessed borosilicate glass sample to 4.94 GPa.

From "Pressure Induced Densification and Compression in a Reprocessed Borosilicate Glass" by Kathryn J. Ham, Yoshio Kono, Parimal J. Patel, Steven M. Kilczewski, and Yogesh K. Vohra, 2018, Materials, 11(1), p. 114. Copyright 2018 by the authors. Reprinted with permission.

The height and width of the sample were found in pixels. The sample height at ambient pressure, H_0 and sample width at ambient pressure, W_0 were used to normalize the sample height, H and the sample width, W so that $\left(\frac{H}{H_0}\right) = 1$ and $\left(\frac{W}{W_0}\right) = 1$ at ambient pressure. For the borosilicate glass sample, the volume was calculated as:

$$V = \pi \left(\frac{W}{2}\right)^2 H$$

Where V is sample volume, W is the width of the cylindrical sample, and H is the height of the cylindrical sample. The height, width, and volume values are plotted in Figure 19.

The dashed line in each of the plots in Figure 20 is only meant as a guide for the eye, and is not representative of a fit of any kind.

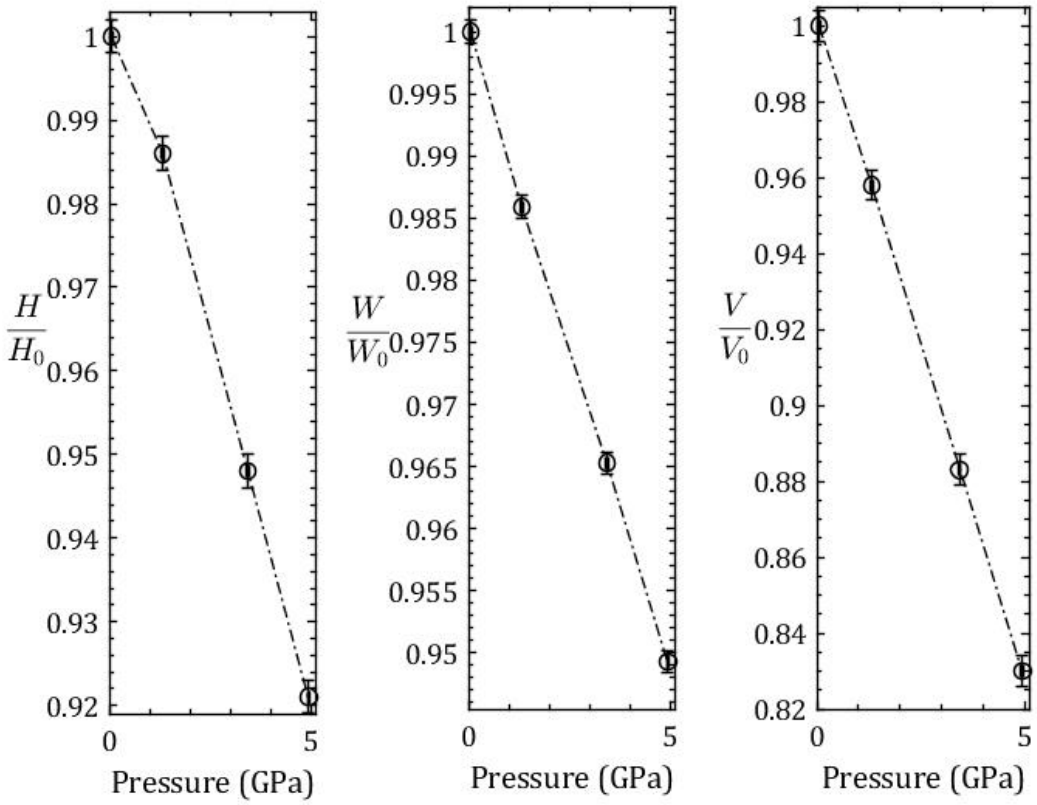

Figure 20. Experimentally obtained sample width change with pressure (W/W_0), sample height change with pressure (H/H_0), and sample volume change with pressure (V/V_0), estimated by white-beam X-ray radiography for the reprocessed borosilicate glass sample.

The bulk modulus of the borosilicate glass sample was found as:

$$B_0 = -V\left(\frac{dP}{dV}\right)_0$$

Giving a B_0 = 30.34 GPa.

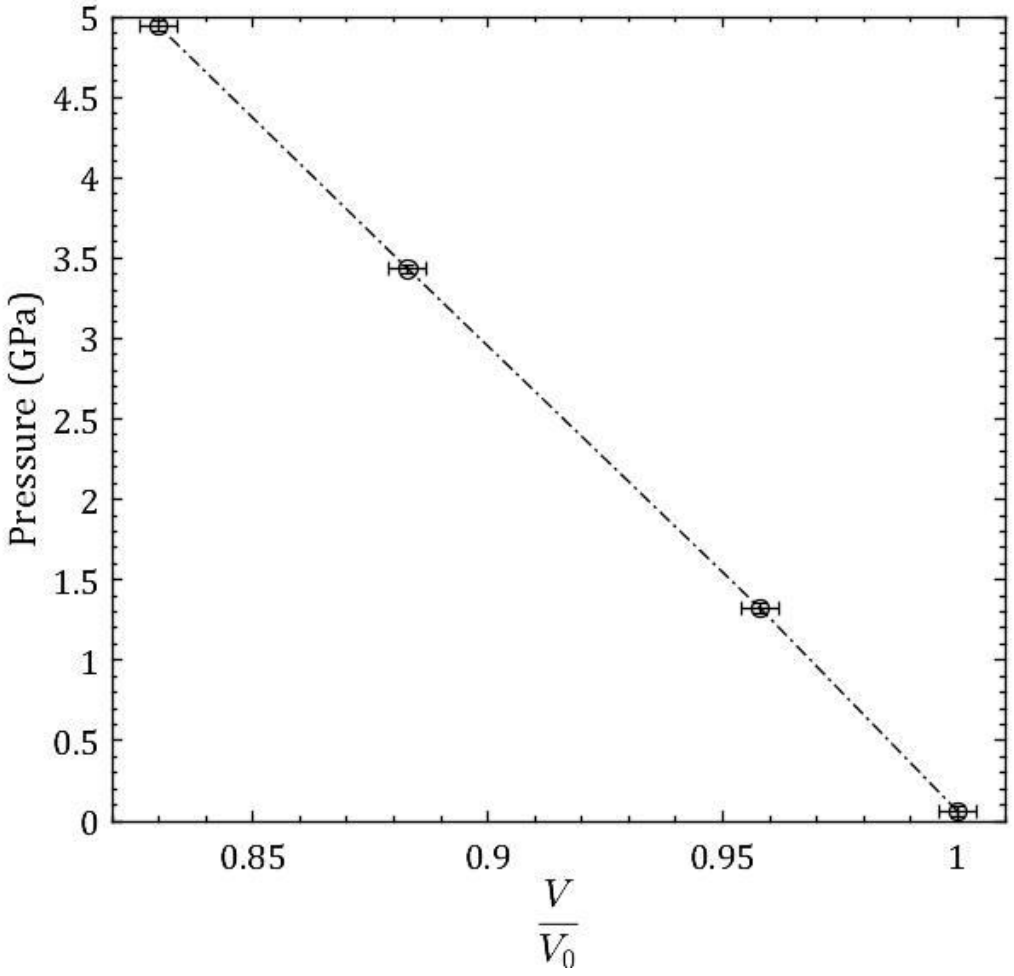

Figure 21. Pressure-Volume (P-V) data or equation of state of reprocessed borosilicate glass obtained by X-ray radiography method. The bulk modulus for the reprocessed borosilicate glass is obtained from the initial compression to 4.94 GPa.

From "Pressure Induced Densification and Compression in a Reprocessed Borosilicate Glass" by Kathryn J. Ham, Yoshio Kono, Parimal J. Patel, Steven M. Kilczewski, and Yogesh K. Vohra, 2018, Materials, 11(1), p. 114. Copyright 2018 by the authors. Reprinted with permission.

The sample of commercial Borofloat has a Young's modulus of E = 63.1 GPa and a Poisson's ratio of ν = 0.18 [2]. Using the equation to relate the bulk modulus to Young's modulus and Poisson ratio:

$$B_0 = \frac{E}{[3(1-2\nu)]}$$

The bulk modulus can be calculated as B_0 = 32.9 GPa. The bulk modulus obtained from this experiment, B_0 = 30.34 GPa gives an 8.1% difference from the bulk modulus obtained from calculation of reference elastic constants [2].

High B Sample

White X-ray radiography measurements were conducted alongside multi-angle EDXD measurements to look at bulk volume changes as the borosilicate glass samples were compressed. At each pressure step, radiography images were taken, as seen in Figure 22 with the gold foil markers (dark lines) providing information about the vertical extent (height) of the sample.

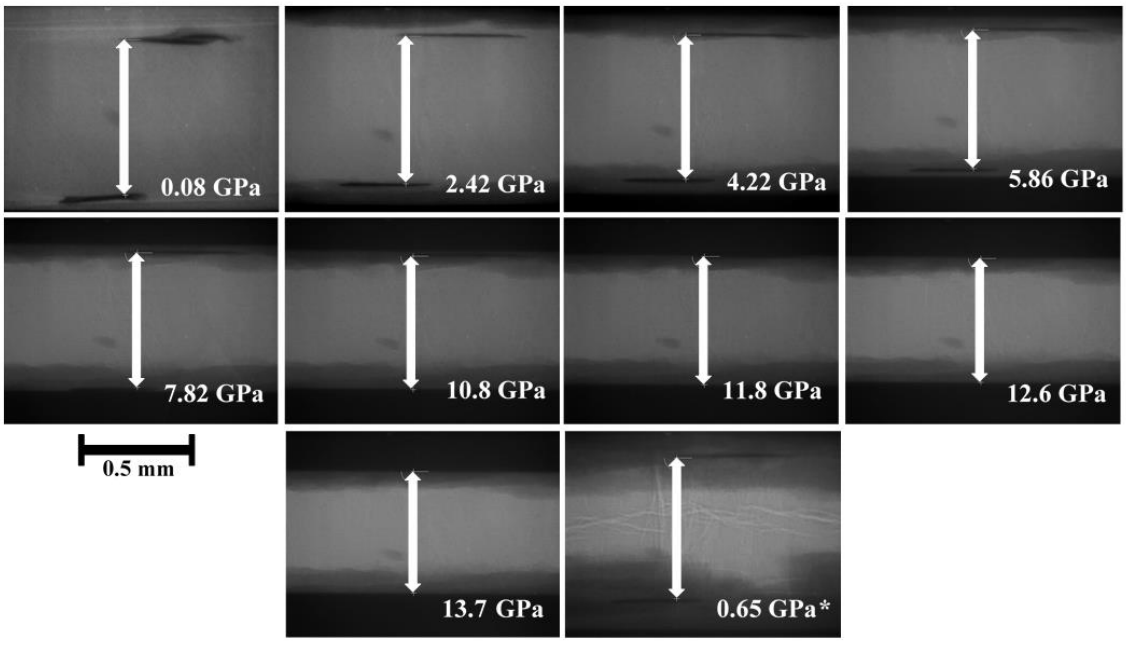

Figure 22. White-beam X-ray radiography images of the sample at increasing pressures and on decompression. The gold foils represented by the dark features represent the vertical extent of the glass sample [47].

From “White-beam X-ray diffraction and radiography studies on high-boron-containing borosilicate glass at high pressures” by K. J. Ham, Y. K. Vohra, Y. Kono, A. A. Wereszczak, and P. Patel, 2017, High Pressure Research, 37, p. 236. Copyright 2017 by Informa UK Limited, trading as Taylor & Francis Group. Reprinted with permission.

The sample height *h* shows an expected decrease as pressure is increased, as shown in Figure 23 with some recovery on decompression, denoted by an open diamond ‘◊.’ The values of $\frac{h}{h_0}$ are shown below in Table 2.

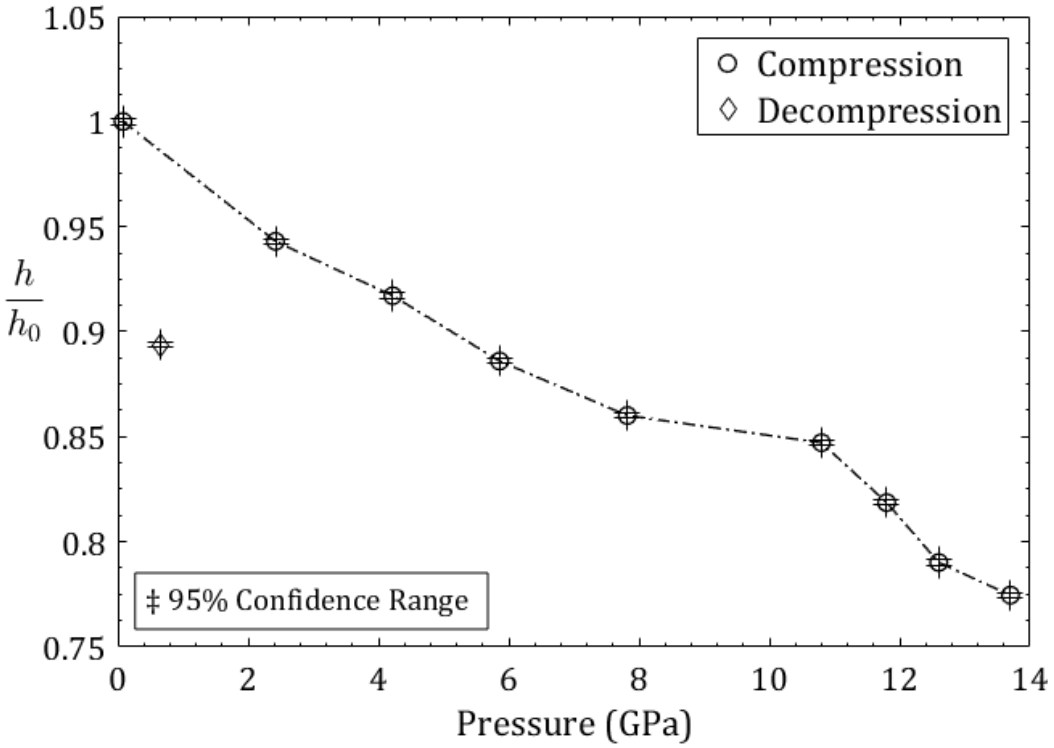

Figure 23. Sample height change with pressure, estimated by white-beam X-ray radiography. The decompression data point after pressure release is also shown as ‘◊.’

From “White-beam X-ray diffraction and radiography studies on high-boron-containing borosilicate glass at high pressures” by K. J. Ham, Y. K. Vohra, Y. Kono, A. A. Wereszczak, and P. Patel, 2017, High Pressure Research, 37, p. 238. Copyright 2017 by Informa UK Limited, trading as Taylor & Francis Group. Adapted with permission.

At 13.7 GPa, the maximum pressure, the sample is compressed by 22.5% in the vertical or the loading direction. Upon decompression, the sample remains compacted, with a reduction in height $\frac{\Delta h}{h_0}$ of 0.894, where h_0 is the initial height of the specimen. This indicates a residual compression of 10.6% along the loading direction. It should be added that the horizontal sample dimension was not able to be measured by radiography due to lack of gold fiducial markers in that direction and hence the Poisson ratio cannot be calculated.

Table 7. Sample height change with pressure, estimated by white-beam X-ray radiography. The decompression data point after pressure release is denoted by '*.'

Pressure (GPa)	L/L_0
0.08	1
2.42	0.943
4.22	0.9171
5.86	0.886
7.82	0.8601
10.8	0.8472
11.8	0.8187
12.6	0.7902
13.7	0.7746
0.65*	0.8938

Raman Spectroscopy

Raman spectroscopy was conducted on a bulk sample of the high B sample and on the recovered glass sample from high-pressure EDXD experiments. Figure 14 shows (top) the recovered borosilicate glass sample in the h-BN cup and (bottom) gold foil on the h-BN cap after compression to 13.7 GPa.

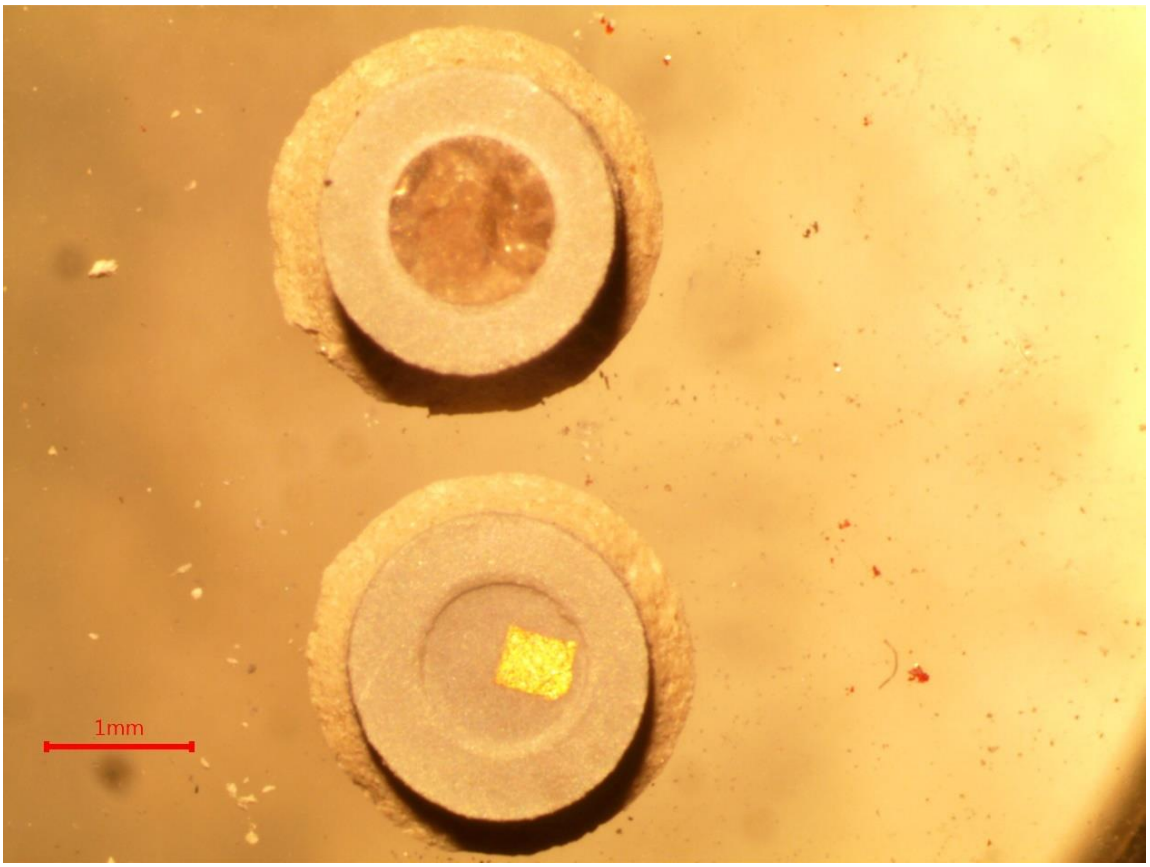

Figure 24. Photomicrograph of (top) the high-boron-content borosilicate glass recovered sample in h-BN cup and (bottom) the h-BN cap and gold foil after compression to 13.7 GPa. The 1 mm scale bar is indicated.

After extraction of the borosilicate glass sample from the h-BN cup, the sample remained intact, although large cracks throughout the sample are seen. The top and bottom of the recovered sample from compression to 13.7 GPa are shown in Figure 24 and Figure 25 respectively.

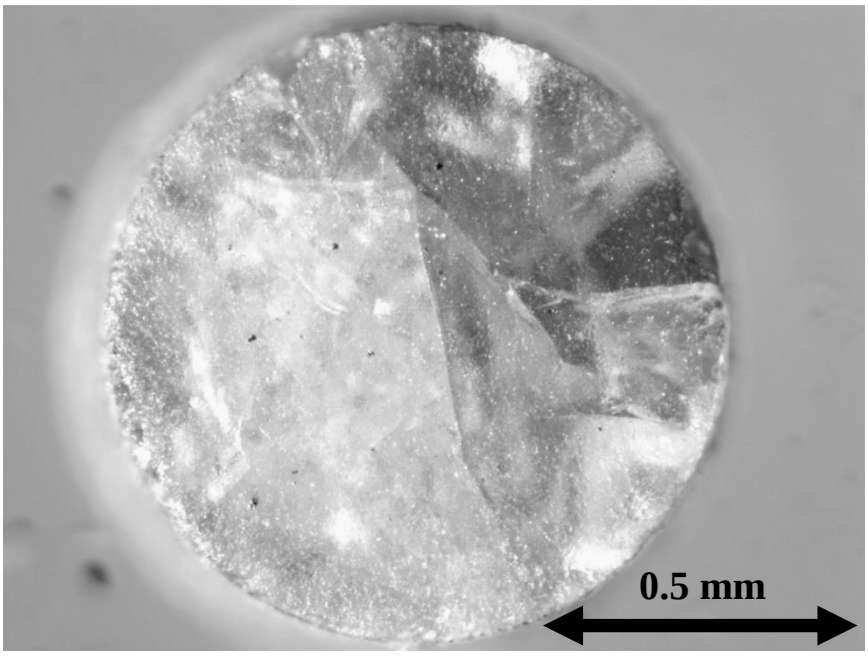

Figure 25. Photomicrograph of the top of the high-boron-content borosilicate glass recovered sample after compression to 13.7 GPa at 32x magnification. The scale bar of 0.5 mm is indicated.

The comparison of the Raman spectra for the High B sample, before and after compression along with the assignment of peaks labeled a - f is shown in Figure 26. The first peak in the Raman spectrum of the starting bulk sample is at 443 cm^{-1} which appears at 465 cm^{-1} in the pressure recovered sample spectrum (Figure 26). This Raman shift corresponds to silicate rings, where an increase in wavenumber corresponds to a decrease in the number of members in the silicate rings [53]. The glass sample went from a network of 5- and 6- membered silicate rings to a network of predominately 4- and 5- membered silicate rings. The peak in the recovered sample spectrum at 602 cm^{-1} (Figure 26) is not seen at all in the bulk sample spectrum and corresponds to small 3-membered silicate rings [53]. This provides further confirmation that the overall silicate ring network shows signs of permanent deformation, shifting from higher coordination to lower coordination

after decompression from a pressure of 13.7 GPa. The peak in the spectrum of the starting bulk sample at 789.9 cm^{-1} appears at 803.3 cm^{-1} in the pressure recovered sample, which has been attributed to four-coordinated boron and boroxol rings (Figure 26) [45,53]. The peak that appears only in the recovered spectrum at 1364.5 cm^{-1} (Figure 26) corresponds to h-BN, which is acceptable since Raman spectroscopy was performed on the recovered glass sample still in the h-BN cup from the PE cell [54]. In addition, an increase in Raman frequency of the four-coordinated boron and boroxol rings from 789.9 to 803 cm^{-1} indicates that the force constant has increased after compression to 13.7 GPa. There is also an increase in frequency of the silicate ring from 443.2 to 465 cm^{-1} indicating a shift from 5- to 6- membered silicate rings to 4- and 5-membered silicate rings. The full width at half maximum (FWHM) of the 443.2 cm^{-1} peak of the bulk sample is 145.2 cm^{-1}, which is wider as compared to the FWHM of the 465 cm^{-1} peak of the recovered bulk sample which was 81.6 cm^{-1}. The sharpening of the peak seen in the recovered bulk sample can be attributed to a more stable rearrangement of 4- and 5- membered silicate rings after decompression from 13.7 GPa.

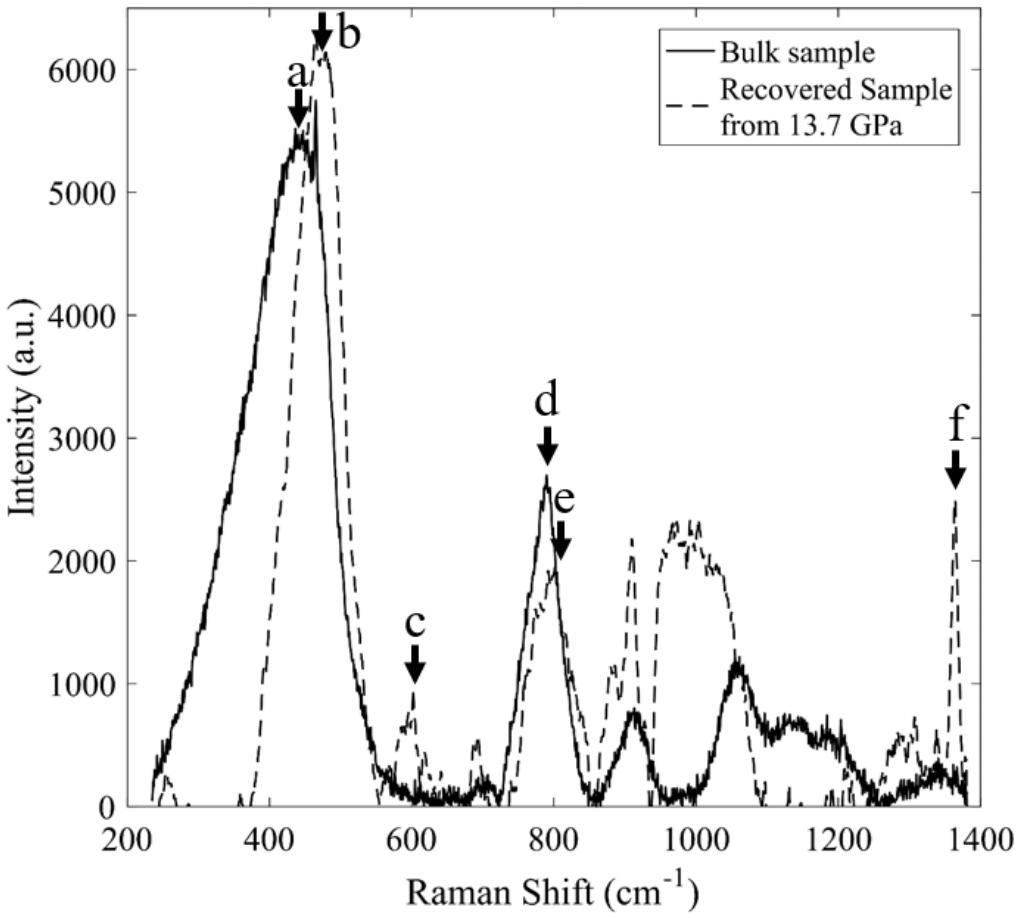

Figure 26. Comparison of Raman spectra of the ambient pressure bulk High B sample and the High B sample recovered from a pressure of 13.7 GPa. The blue-shift and intensity changes of several Raman bands are apparent from this comparison. The peaks' assignments are denoted: (a) ambient pressure network of 5- and 6-membered silicate rings, (b) recovered sample network of 4- and 5-membered silicate rings, (c) recovered sample network of 3-membered silicate rings, (d) ambient pressure four-coordinated boron, (e) recovered sample four-coordinated boron, and (f) hexagonal boron nitride peak from the sample holder [47].

From "White-beam X-ray diffraction and radiography studies on high-boron-containing borosilicate glass at high pressures" by K. J. Ham, Y. K. Vohra, Y. Kono, A. A. Wereszczak, and P. Patel, 2017, High Pressure Research, 37, p. 241. Copyright 2017 by Informa UK Limited, trading as Taylor & Francis Group. Reprinted with permission

The comparison of the Raman spectra before and after compression for the reprocessed Borofloat sample, along with the assignment of peaks labeled a - d is shown

in Figure 27. The first peak in the Raman spectrum of the starting bulk sample is at 460.1 cm^{-1} which appears at 465.2 cm^{-1} in the pressure recovered sample spectrum (Figure 27). This Raman shift corresponds to silicate rings, where an increase in wavenumber corresponds to a decrease in the number of members in the silicate rings [53]. The glass sample went from a network of 5- and 6- membered silicate rings to a network of predominately 4- and 5- membered silicate rings. The peak in the recovered sample spectrum at 627.7 cm^{-1} (Figure 27) is not seen at all in the bulk sample spectrum and corresponds to small 3-membered silicate rings [53]. This provides further confirmation that the overall silicate ring network shows signs of permanent deformation, shifting from higher coordination to lower coordination after decompression from a pressure of 12.2 GPa. The peak in the spectrum of the starting bulk sample at 798.8 cm^{-1} appears at 804.9 cm^{-1} in the pressure recovered sample, which has been attributed to four-coordinated boron (Figure 27) [45,53]. In addition, an increase in Raman frequency of the four-coordinated boron from 798.8 to 804.9 cm^{-1} indicates that the force constant has increased after compression to 13.7 GPa. There is also an increase in frequency of the silicate ring from 460.1 to 465.2 cm^{-1} indicating a shift from 5- to 6- membered silicate rings to 4- and 5-membered silicate rings.

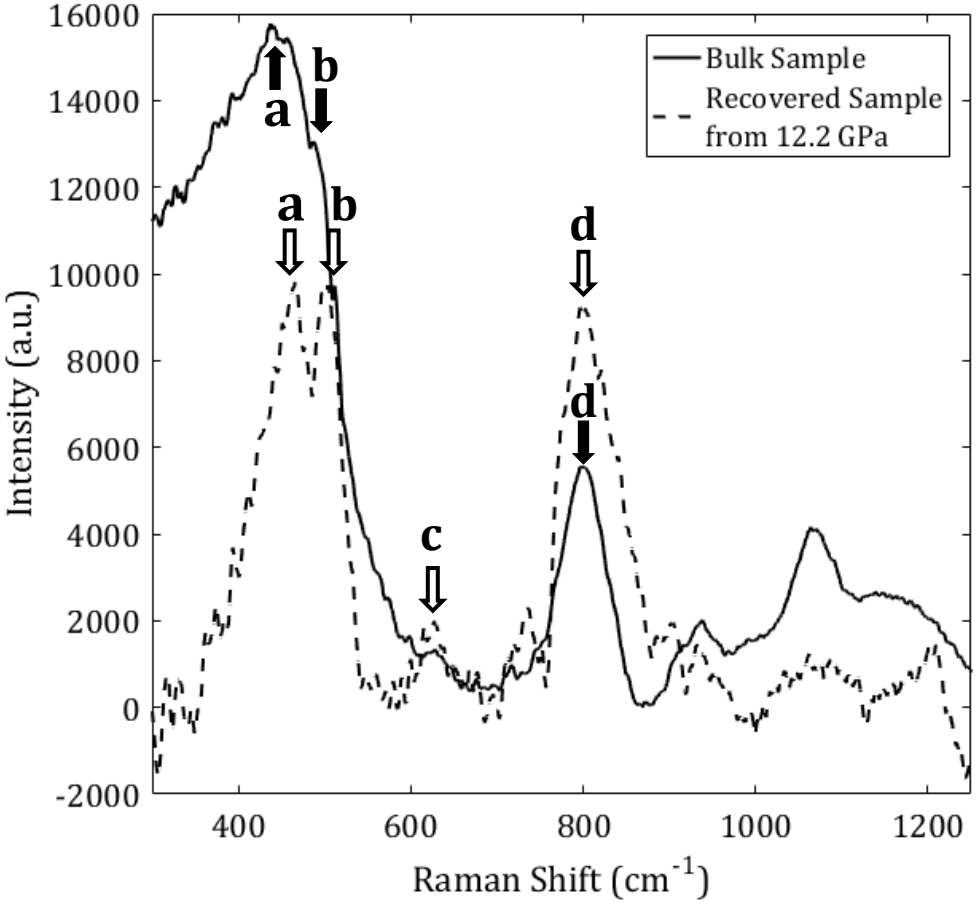

Figure 27. Raman of the reprocessed Borofloat sample before and after compression to 12.2 GPa.

Table 8. Summary of Raman results for the borosilicate glass samples.

	Bending mode of Si-O-Si mode in 5-6 membered rings	Bending mode of Si-O-Si mode in 4-5 membered rings	Bending mode of Si-O-Si mode in 3 membered rings	Boroxol rings- ring breathing mode	Stretching vibrations of nonbridge bonds of Q^2 structural units	Stretching vibrations of nonbridge bonds of Q^3 structural units
Recovered reprocessed Borofloat (from 12.2 GPa) Raman Shift (cm^{-1})	465.2	5 05	627.7	804.9	938.1	1076

Recovered High B (from 13.7 GPa) Raman Shift (cm^{-1})	465	-	602	803.3	909.7	1002.7
Low B borosilicate Sample Raman shift (cm^{-1})	479	-	-	801.7	948.4	1059.7
Bulk reprocessed Borofloat Raman shift (cm^{-1})	460.1	494.9	-	798.8	932.3	1065
High B borosilicate Sample Raman shift (cm^{-1})	453	-	-	789	913.3	1061

The results from the Raman spectroscopy studies show that for the bulk borosilicate samples there is a shift towards lower number membered silicate rings with a decreasing B_2O_3 content. Also, when comparing the bulk samples with the high pressure recovered samples there is evidence of permanent compression in the silicate and boroxol rings for both the High B sample and the reprocessed Borofloat sample (

Table 8).

Floatation Density Measurements

Flotation density measurements were conducted on the three borosilicate glass samples, each before and after exposure to high pressure conditions to look for signs of permanent deformation by a change in density between the pre and post pressure exposed

samples. The density measurements for the bulk samples are seen in Table 9, Table 11, and Table 13. The density measurements for the high pressure recovered samples are seen in Table 10, Table 12, and Table 14. Each table shows the amount of LMT, water added, the total volume, and the density. When the density of the sample matches the density of the liquid and does not float or sink, the fluid density is equivalent to the density of the sample (shown in the tables bolded).

Table 9. Density measurement for the bulk High B sample.

Trial	LMT added (mL)	Water added (μL)	Total Volume (mL)	Density (gm/cc)
1	3	0	3.000	2.950
2	0	900.0	3.900	2.500
3	0	278.6	4.179	2.400
4	0	60.6	4.239	2.380
5	0	94.2	4.333	2.350
6	0	98.5	4.432	2.320
7	0	68.2	4.500	2.300
8	0	34.9	4.535	2.290
9	0	35.4	4.570	2.280
10	0	36.0	4.606	2.270
11	0	36.6	4.643	2.260
12	0	37.1	4.680	2.250
13	0	37.7	4.718	2.240
14	0	38.4	4.756	2.230
15	0	39.0	4.795	2.220
16	0	39.6	4.835	2.210
17	0	4.0	4.839	2.209
18	0	4.0	4.843	2.208
19	0	4.0	4.847	**2.207**

Table 10. Density measurement for the High B sample recovered from 11.6 GPa.

Trial	LMT added (mL)	Water added (µL)	Total Volume (mL)	Density (gm/cc)
1	3	0	3.000	2.950
2	0	900.0	3.900	2.500
3	0	134.5	4.034	2.450
4	0	56.4	4.091	2.430
5	0	28.8	4.120	2.420
6	0	29.2	4.149	2.410
7	0	2.9	4.152	2.409
8	0	2.9	4.155	2.408
9	0	5.9	4.161	2.406
10	0	5.9	4.167	2.404
11	0	11.9	4.179	2.400
12	0	30.1	4.209	2.390
13	0	30.5	4.239	2.380
14	0	15.4	4.255	2.375
15	0	6.2	4.261	2.373
16	0	9.3	4.270	2.370
17	0	6.2	4.276	2.368
18	0	6.3	4.283	2.366
19	0	6.3	4.289	2.364
20	0	6.3	4.295	2.362
21	0	6.3	4.301	**2.360**

Table 11. Density measurement for the bulk Low B Sample.

Trial	LMT added (mL)	Water added (µL)	Total Volume (mL)	Density (gm/cc)
1	3.000	0	3.000	2.950
2	0	900.0	3.900	2.500
3	0	278.6	4.179	2.400
4	0	60.6	4.239	2.380
5	0	94.2	4.333	2.350
6	0	98.5	4.432	2.320
7	0	68.2	4.500	2.300
8	0	34.9	4.535	2.290
9	0	35.4	4.570	2.280
10	0	36.0	4.606	2.270

11	0	36.6	4.643	2.260
12	0	37.1	4.680	2.250
13	0	37.7	4.718	2.240
14	0	38.4	4.756	2.230
15	0	3.9	4.760	2.229
16	0	3.9	4.767	2.228
17	0	3.9	4.768	2.227
18	0	3.9	4.772	2.226
19	0	3.9	4.776	2.225
20	0	3.9	4.779	2.224
21	0	3.9	4.783	2.223
22	0	3.9	4.787	2.222
23	0	3.9	4.791	2.221
24	0	3.9	4.795	2.220
25	0	3.9	4.799	2.219
26	0	3.9	4.803	2.218
27	0	3.9	4.807	2.217
28	0	4.0	4.811	**2.216**

Table 12. Density measurement for the Low B Sample recovered from 10.9 GPa.

Trial	**LMT added (mL)**	**Water added (µL)**	**Total Volume (mL)**	**Density (gm/cc)**
1	3.000	0	3.000	2.950
2	0	900.0	3.900	2.500
3	0	278.6	4.179	2.400
4	0	30.1	4.209	2.390
5	0	30.5	4.239	2.380
6	0	4.2	4.245	2.378
7	0	9.3	4.255	2.375
8	0	9.3	4.264	2.372
9	0	6.2	4.270	2.370
10	0	3.1	4.273	2.369
11	0	6.3	4.279	2.367
12	0	6.3	4.286	2.365
13	0	6.3	4.292	2.363
14	0	6.3	4.298	2.361
15	0	3.2	4.301	2.360
16	0	6.3	4.308	2.358

17	0	6.4	4.314	2.356
18	0	6.4	4.321	2.354
19	0	6.4	4.327	2.352
20	0	6.4	4.333	2.350
21	0	6.4	4.340	2.348
22	0	3.2	4.343	2.347
23	0	3.2	4.346	2.346
24	0	3.2	4.349	2.345
25	0	3.2	4.356	2.344
26	0	3.2	4.359	2.343
27	0	3.2	4.362	2.342
28	0	6.5	4.396	2.340
29	0	6.5	4.375	**2.338**

Table 13. Density measurement for the bulk Borofloat sample.

Trial	**LMT added (mL)**	**Water added (µL)**	**Total Volume (mL)**	**Density (gm/cc)**
1	5	0	5.000	2.950
2	0	1500.0	6.500	2.500
3	0	1000.0	7.500	2.300
4	0	300.0	7.800	2.250
5	0	62.9	7.869	2.240
6	0	63.9	7.927	2.230
7	0	12.9	7.940	2.228
8	0	25.9	7.966	2.224
9	0	6.5	7.972	2.223
10	0	6.5	7.978	2.222
11	0	6.5	7.985	2.221
12	0	6.5	7.992	2.220
13	0	6.7	7.998	2.219
14	0	26.3	8.025	**2.215**

Table 14. Density measurement for the 12.45% B_2O_3 borosilicate glass sample recovered from 11.8 GPa.

Trial	**LMT added (mL)**	**water added (µL)**	**Total Volume (mL)**	**Density (gm/cc)**

1	3	0	3.000	2.950
2	0	900.0	3.900	2.500
3	0	278.6	4.179	2.400
4	0	56.4	4.091	2.430
5	0	58.0	4.149	2.410
6	0	59.7	4.209	2.390
7	0	30.5	4.239	2.380
8	0	30.7	4.270	2.370
9	0	3.1	4.273	2.369
10	0	3.1	4.276	2.368
11	0	3.1	4.279	**2.367**

The density change for the High B sample:

$$\frac{\rho_0}{\rho} = \frac{V}{V_0} = \frac{2.207\frac{gm}{cc}}{2.360\frac{gm}{cc}} = 0.9352 \rightarrow \mathbf{93.52}\%$$

The density change for the 12.45% B_2O_3 borosilicate glass sample:

$$\frac{\rho_0}{\rho} = \frac{V}{V_0} = \frac{2.215\frac{gm}{cc}}{2.367\frac{gm}{cc}} = 0.9358 \rightarrow \mathbf{93.58}\%$$

The density change for the Low B sample:

$$\frac{\rho_0}{\rho} = \frac{V}{V_0} = \frac{2.216\frac{gm}{cc}}{2.338\frac{gm}{cc}} = 0.9478 \rightarrow \mathbf{94.78}\%$$

Where ρ_0 is the starting sample density, ρ is the sample density after recovery from high-pressure experiments, V_0 is the initial sample volume, and V is the sample volume after recovery from high-pressure experiments.

Table 15. Density measurements for the borosilicate glass samples.

	High B (17.57% B_2O_3)		**Reprocessed Borofloat (12.45% B_2O_3)**		**Low B (8.46% B_2O_3)**	
	Bulk	Recovered	Bulk	Recovered	Bulk	Recovered
ρ (gm/cc)	2.207	2.36	2.215	2.367	2.216	2.338
$\frac{V}{V_o}$	93.52%		93.67%		94.78%	
P_{max} (GPa)	11.6		11.8		10.9	

From these density measurements performed on the three borosilicate glass samples of varying B_2O_3 concentrations, there is a correlation between bulk sample density and percentage of B_2O_3, where a higher B_2O_3 concentration corresponds to a lower sample volume change (Table 15).

BULK METALLIC GLASS STRUCTURAL STUDIES

Structural Studies

Energy-Dispersive X-Ray Diffraction

White-beam energy-dispersive X-ray diffraction was conducted on a sample of Vit 106a to look at the pressure and temperature dependence of the structure factor, *S(q)* and the reduced pair distribution factor, *G(r)* (Figure 28). The structure factor *S(q)* for the bulk metallic glass sample is shown in Figure 28B. The First Sharp Diffraction Peak (FSDP) in the initial ambient *S(q)* spectrum (Figure 28B) appears at $q = 2.58 \pm 0.01$ Å^{-1} and moves to higher *q*-values with increasing pressure. The FSDP position (Å^{-1}) is plotted for increasing pressure (GPa) in Figure 29, with peak values in Table 16. The shift of the FSDP peak indicates intermediate range structural changes in the glass sample [57–60].

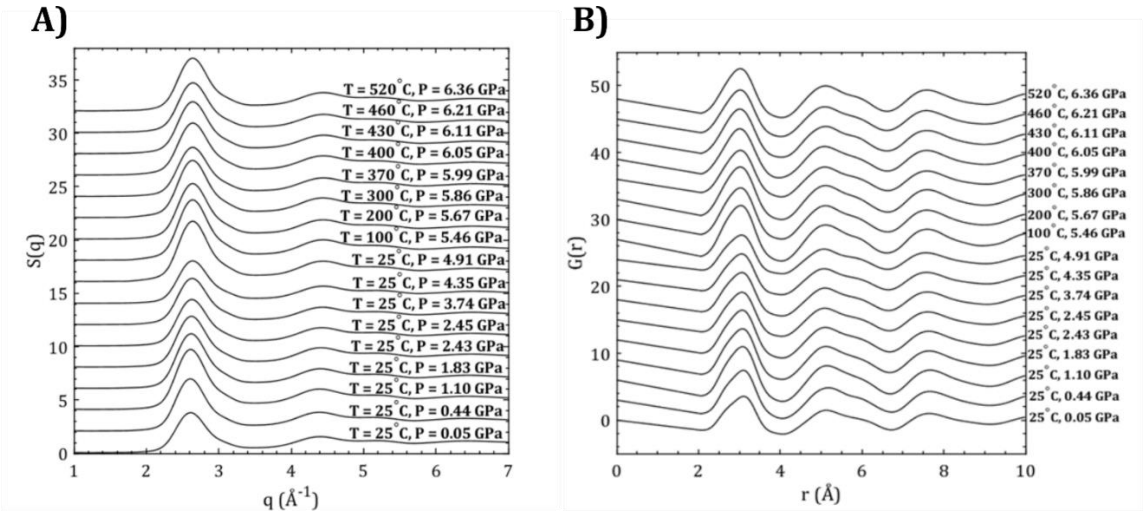

Figure 28. A) The structure factor, S(q) at increasing pressure and temperature for Vit 106a. B) The reduced pair distribution function, G(r) for Vit 106a.

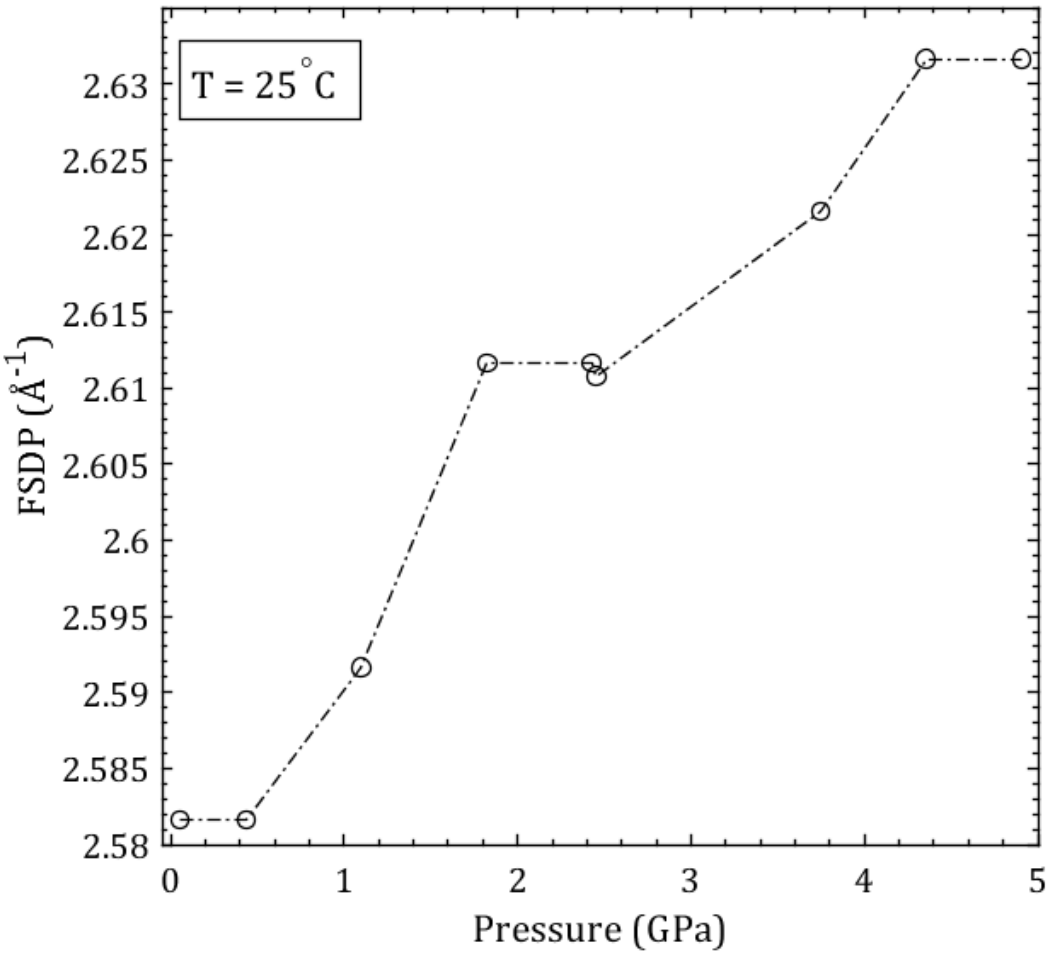

Figure 29. The First Sharp Diffraction Peak (FSDP) for the bulk metallic glass at ambient temperature and increasing pressure. The dotted line is a guide for the eye.

Table 16. Measured First Sharp Diffraction Peak (FSDP) shift in the S(q) spectra at various pressures for the bulk metallic glass sample at T = 25°C.

Sample Pressure (GPa)	FSDP ($Å^{-1}$)
0.05	2.58 ± 0.01
0.44	2.58 ± 0.01
1.10	2.59 ± 0.01
1.83	2.61 ± 0.01
2.43	2.61 ± 0.01
2.45	2.61 ± 0.01

3.75	2.62 ± 0.01
4.35	2.63 ± 0.01
4.91	2.63 ± 0.01

The first prominent peak in the reduced pair distribution function *G(r)*, r_2 (Figure 28A) appears at 3.10 ± 0.02 Å and remains consistent in shape up to pressures of 4.91 GPa at ambient temperature (Figure 28A). There is a shoulder on the left side of the first prominent Gaussian peak, r_2 which is seen at 2.52 ± 0.13 Å at ambient conditions. This shoulder disappears as soon as the sample is heated (Figure 28A), and the symmetrizing of the first prominent Gaussian peak is seen at the first temperature step at 100°C and 5.46 GPa. All the internuclear distances at various pressures at ambient temperature are summarized in Table 17. The second prominent Gaussian peak, r_3 seen at 5.12 ± 0.04 Å (Figure 28A) at ambient temperature and pressure decreases, as is expected when pressure is applied to the sample. The shoulder on the second prominent Gaussian peak r_4 seen at 6.07 ± 0.13 Å (Figure 28A) at ambient temperature and pressure decreases as well as pressure is applied to the sample. The third prominent Gaussian peak r_5 seen at 7.64 ± 0.03 Å (Figure 28A) at ambient temperature and pressure decreases as well as pressure is applied to the sample.

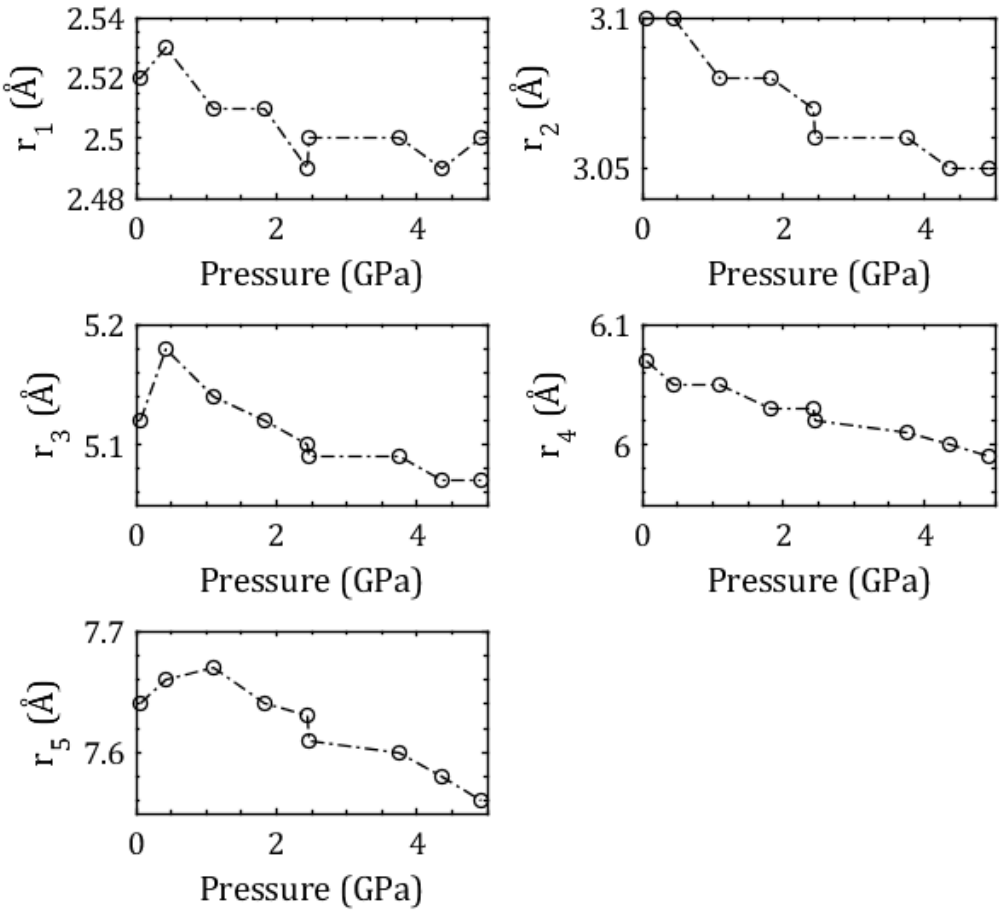

Figure 30. The peaks in the reduced pair distribution function G(r) at ambient temperature, shift with pressure. The dashed line is used to guide the eye and is not a fit.

Table 17. Various measured bond-distances in the bulk metallic glass sample at various pressures and ambient temperature obtained from the reduced pair distribution function G(r).

Pressure (GPa)	r_1 (Å)	r_2 (Å)	r_3 (Å)	r_4 (Å)	r_5 (Å)
0.05	2.52 ± 0.13	3.10 ± 0.02	5.12 ± 0.04	6.07 ± 0.13	7.64 ± 0.03
0.44	2.53 ± 0.13	3.10 ± 0.06	5.18 ± 0.04	6.05 ± 0.15	7.66 ± 0.03
1.10	2.51 ± 0.17	3.08 ± 0.07	5.14 ± 0.05	6.05 ± 0.15	7.67 ± 0.03
1.83	2.51 ± 0.15	3.08 ± 0.07	5.12 ± 0.04	6.03 ± 0.16	7.64 ± 0.03

2.43	2.49 ± 0.87	3.07 ± 0.17	5.10 ± 0.05	6.03 ± 0.13	7.63 ± 0.03
2.45	2.50 ± 0.19	3.06 ± 0.06	5.09 ± 0.04	6.02 ± 0.14	7.61 ± 0.03
3.75	2.50 ± 0.15	3.06 ± 0.06	5.09 ± 0.04	6.01 ± 0.12	7.60 ± 0.03
4.35	2.49 ± 0.16	3.05 ± 0.05	5.07 ± 0.04	6.00 ± 0.12	7.58 ± 0.03
4.91	2.50 ± 0.12	3.05 ± 0.05	5.07 ± 0.04	5.99 ± 0.10	7.56 ± 0.03

White-Beam Radiography

The Vit 106a sample radiography images are shown in Figure 31 at ambient temperature, T = 25°C and increasing pressure to a maximum pressure of 4.91 GPa. The darker area in the center of each radiograph is the Vit 106a sample and the lighter area around the sample is the h-BN cylinder that the sample sits in (Figure 31). As seen by eye, the sample does not appear to change dramatically as pressure is applied, which makes the radiography analysis discussed in Figure 11 important to understand the high-pressure, high-temperature bulk structural changes the sample undergoes. Figure 32 and Table 18 show the $\frac{V}{V_0}$ behavior of the Vit 106a sample as it goes to high-pressure at ambient temperature.

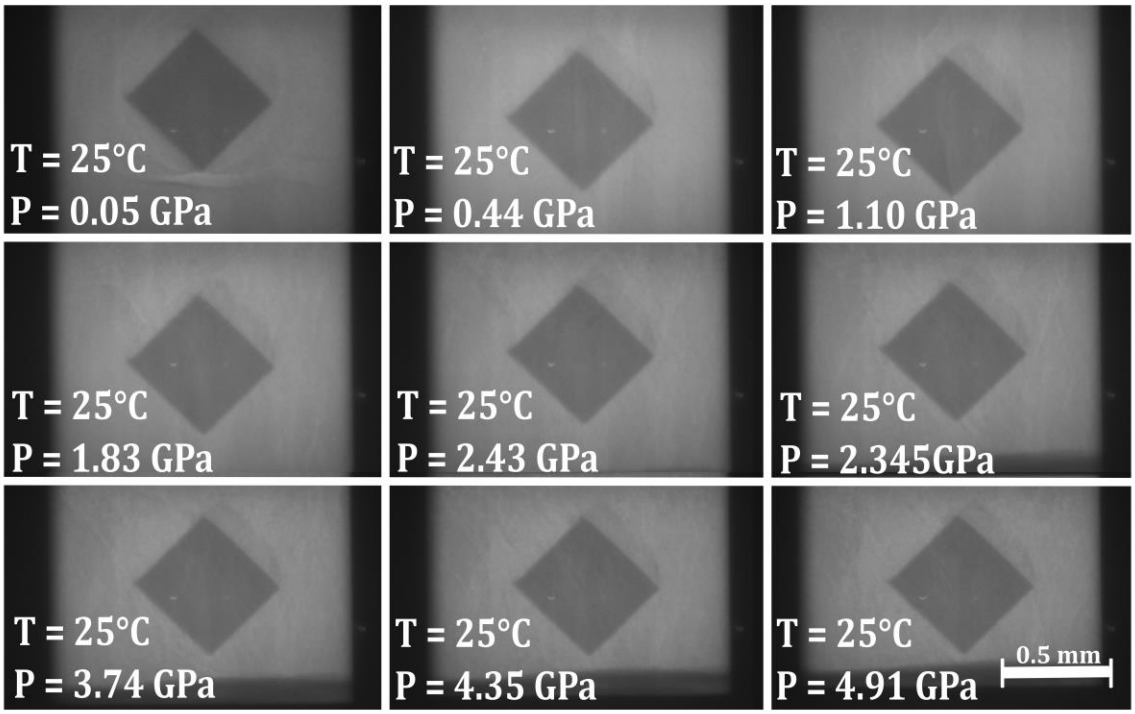

Figure 31. Radiography images of the bulk metallic glass sample at ambient temperature and increasing pressure.

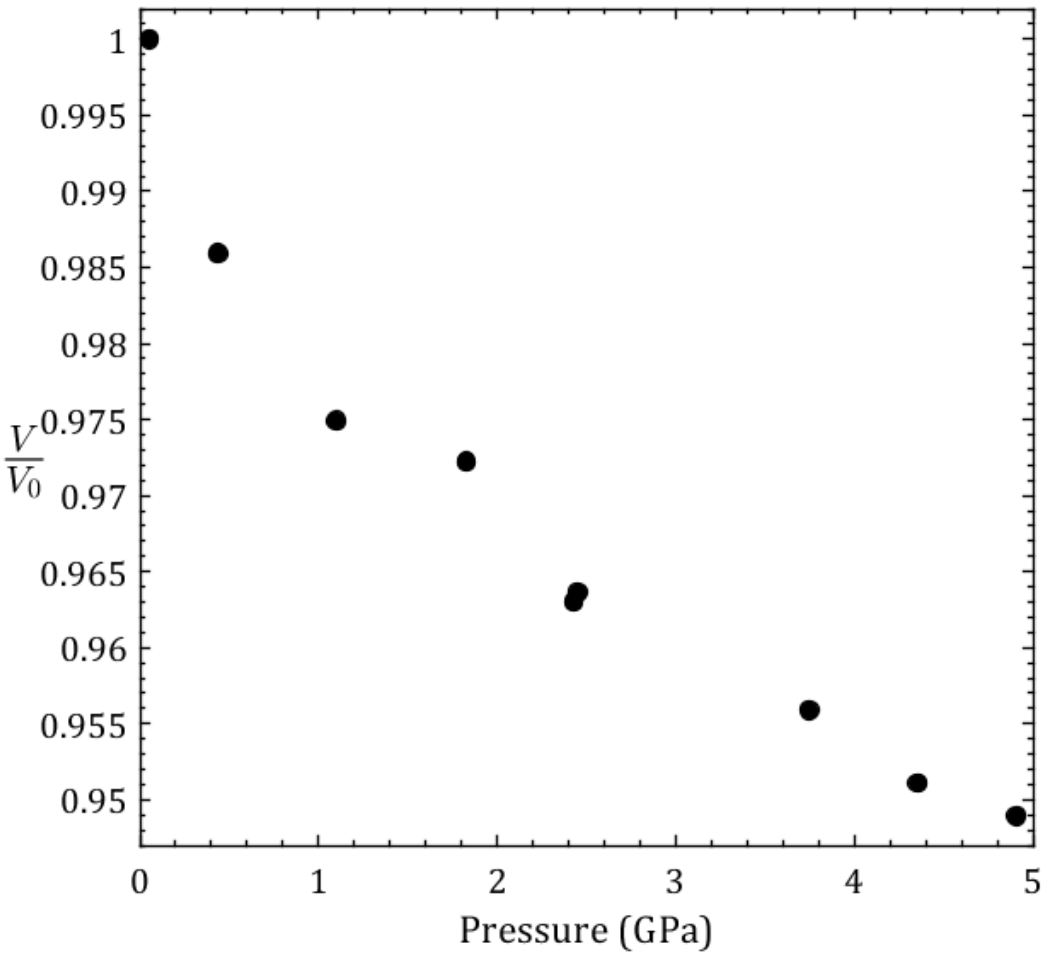

Figure 32. V/V_0 for the bulk metallic glass sample at ambient temperature and increasing pressure.

Table 18. V/V_0 for the bulk metallic glass sample at ambient temperature and increasing pressure.

Pressure (GPa)	V/V_0
0.053	1
0.44	0.9859
1.10	0.9752
1.83	0.9722
2.43	0.9640
2.45	0.9652
3.75	0.9578

4.35	0.9531
4.91	0.9504

At the pressure of 4.91 GPa the sample is held at a constant oil pressure, 8000 psi and the temperature is incrementally increased to 800°C. The radiography images are seen in Figure 33. A large volume collapse is seen at 460°C and 6.21 GPa in Figure 34, Table 19.

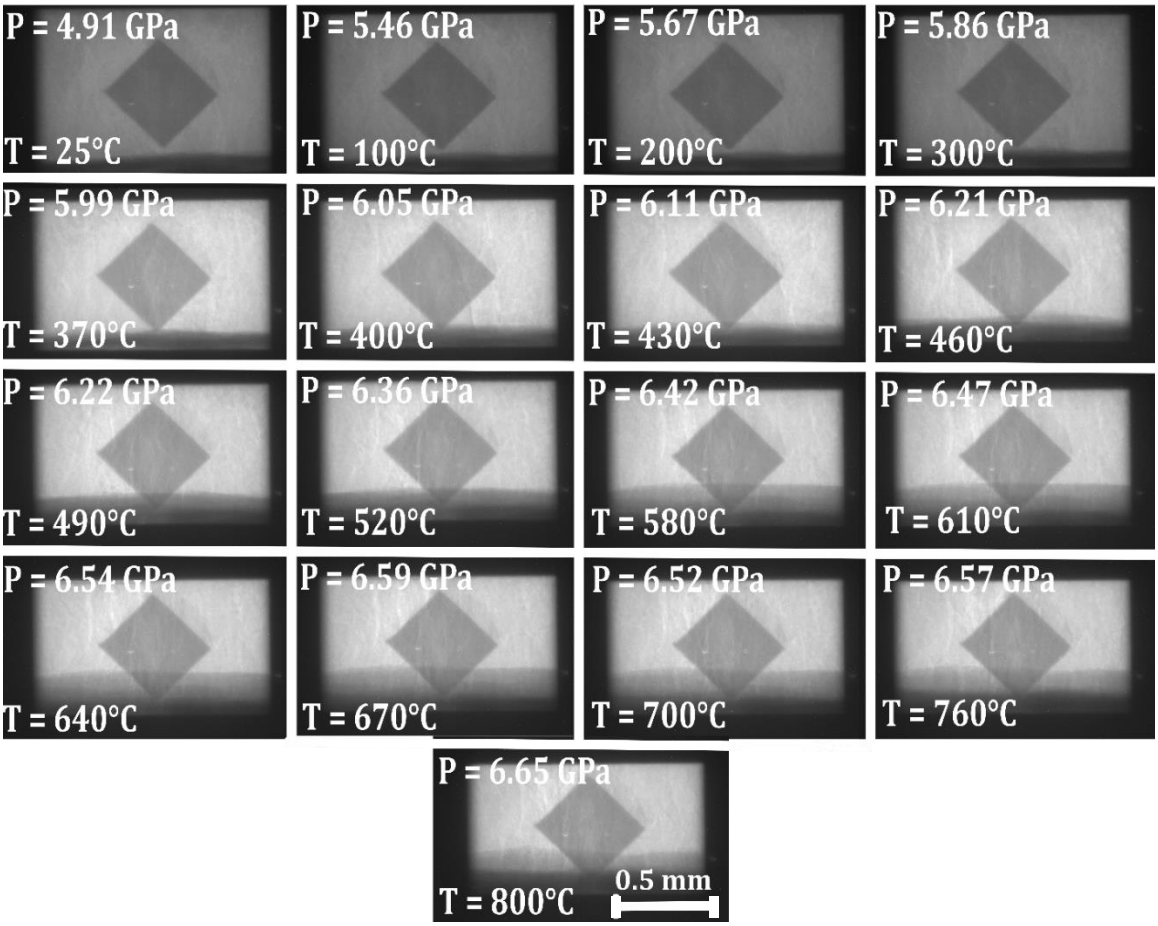

Figure 33. Radiography images of the bulk metallic glass sample at increasing pressure and constant oil pressure, P = 8000 psi.

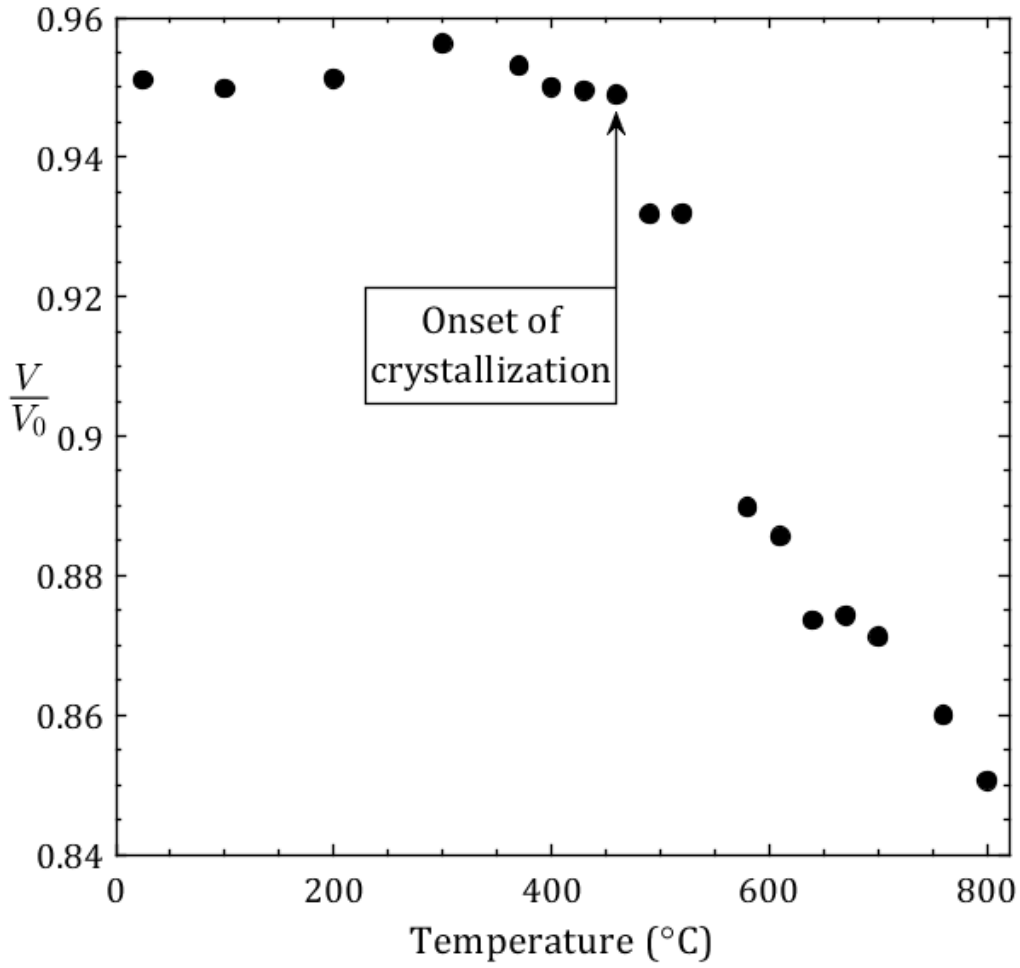

Figure 34. V/V_0 for the bulk metallic glass sample at increasing temperature and constant oil pressure, P = 8000 psi.

Table 19. V/V_0 for the bulk metallic glass sample at increasing temperature and constant oil pressure, P = 8000 psi.

Temp (°C)	Pressure (GPa)	V/V_0
25	4.91	0.9511
100	5.46	0.9498
200	5.67	0.9513
300	5.86	0.9563
370	5.99	0.9531
400	6.05	0.9501
430	6.11	0.9495

460	6.21	0.9490
490	6.22	0.9318
520	6.36	0.9319
580	6.42	0.8898
610	6.47	0.8856
640	6.54	0.8736
670	6.59	0.8742
700	6.52	0.8712
760	6.57	0.8600
800	6.65	0.8506

Crystal Structure

At 800°C the sample is fully crystallized, and the cooled and decompressed ambient EDXD spectrum is seen in Figure 35 with the five predicted equilibrium phases: Zr_3Al_2 (●), Zr_2Cu (♦), Zr_4Al_3 (╋), Zr_2Ni (▼), and ZrCu (★) marked in the figure [61].

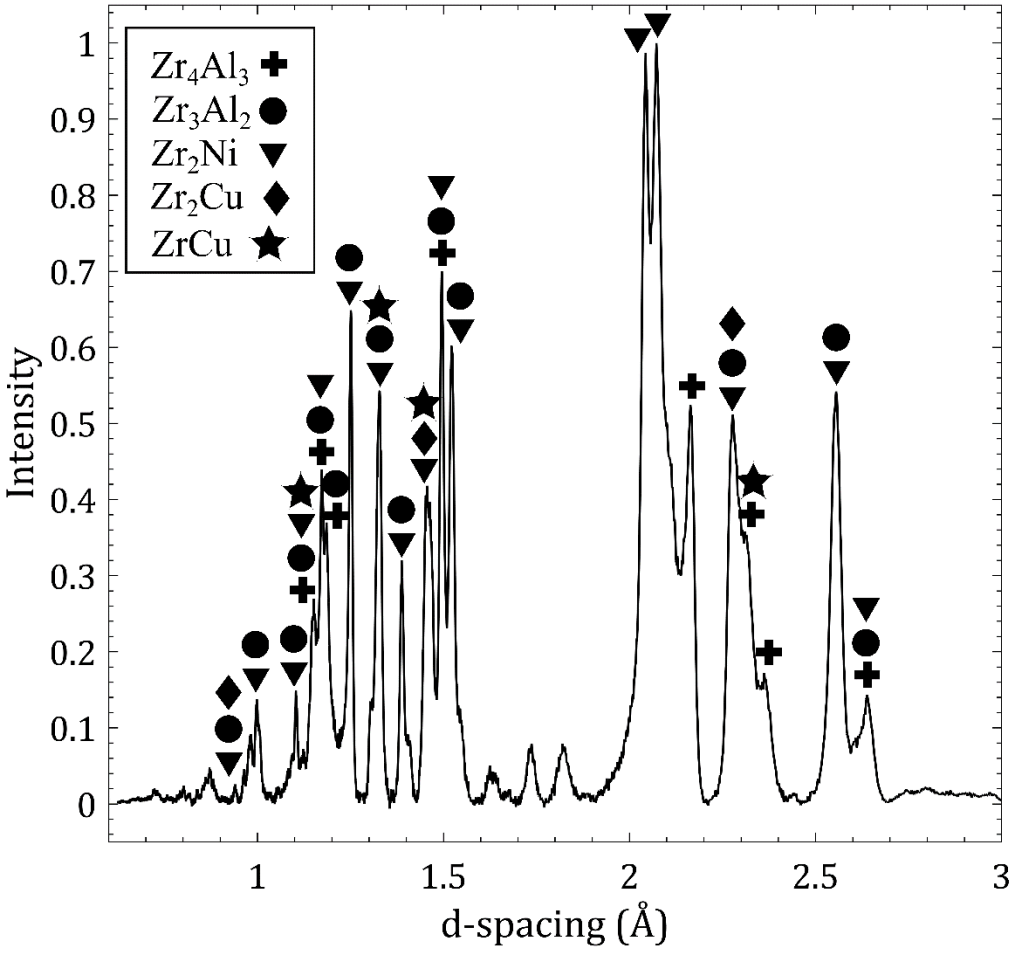

Figure 35. Crystallized EDXD spectrum of the bulk metallic glass sample at $2\theta = 9°$ at ambient conditions after heating to 800°C.

The crystal structure parameters used to assign peaks in Figure 35 are seen below:

Zr_3Al_2, space group #136 ($P4_2/mmm$), a = 0.763 nm, c = 0.6998 nm [62].

Zr_2Cu, space group #139 (I_4/mmm), a = 0.3218 nm, c = 1.118 nm [62].

Zr_4Al_3, space group #191 (P6/mmm), a = 0.5433 nm, c = 0.539 nm [63].

Zr_2Ni, space group #140 (I_4/mcm), a = 0.6486 nm, c = 0.5280 nm [64].

ZrCu space group #221 ($Pm\bar{3}m$), a = 0.3429 nm [65].

Crystallization Temperature Studies

Constant rate heating experiments were conducted on a sample of Zr-based BMG, Vit 106a to look at the effect that high pressure and heating rate have on the sample's crystallization temperature. These experiments were conducted at Beamline 16-BM-B at The Advanced Photon Source using a Paris-Edinburgh Press. The heating rates and pressures investigated in this work are listed in Table 20.

Table 20. Constant rate heating experimental details with heating rates and pressures.

Heating Rate (°C/min)	Pressure (GPa)
6.0	6.38
6.0	5.67
6.0	5.00
6.0	4.34
6.0	3.49
6.0	3.14
6.0	3.01
6.0	2.26
6.0	1.75
6.0	1.49
2.4	7.06
2.4	5.95
2.4	5.84
2.4	4.83
2.4	2.47
2.4	1.45
1.2	5.48
1.2	4.89
1.2	4.75
1.2	4.70
1.2	2.46

Each sample was heated to 350°C from room temperature and then ramp heated at either 1.2, 2.4, or 6.0°C/min until 800°C, then brought to ambient temperature and pressure, and a long final ambient EDXD scan was taken.

Figure 36 shows 999 stacked EDXD spectra for the bulk metallic glass sample at 2.44 GPa, with a constant 1.20°C/min heating ramp between the starting and ending temperatures. The three temperatures shown in Figure 36 are the heating ramp starting temperature (353.2°C), the onset of crystallization temperature (470.4°C), and the heating ramp end temperature (800.9°C). The initial BMG sample is amorphous, as seen from the broad EDXD features from 353.2°C to 470.4°C. After the heating ramp reaches the ending temperature (800.9°C), it is held at a constant temperature for ~1 hour, with no apparent structural changes occurring. The color bar on the right of Figure 36 indicates the intensity, with blue = less intense to yellow = higher intensity. The onset of crystallization in Vit 106a is apparent in Figure 36 as the sudden appearance of crystalline peaks, indicated as thin lines of yellow.

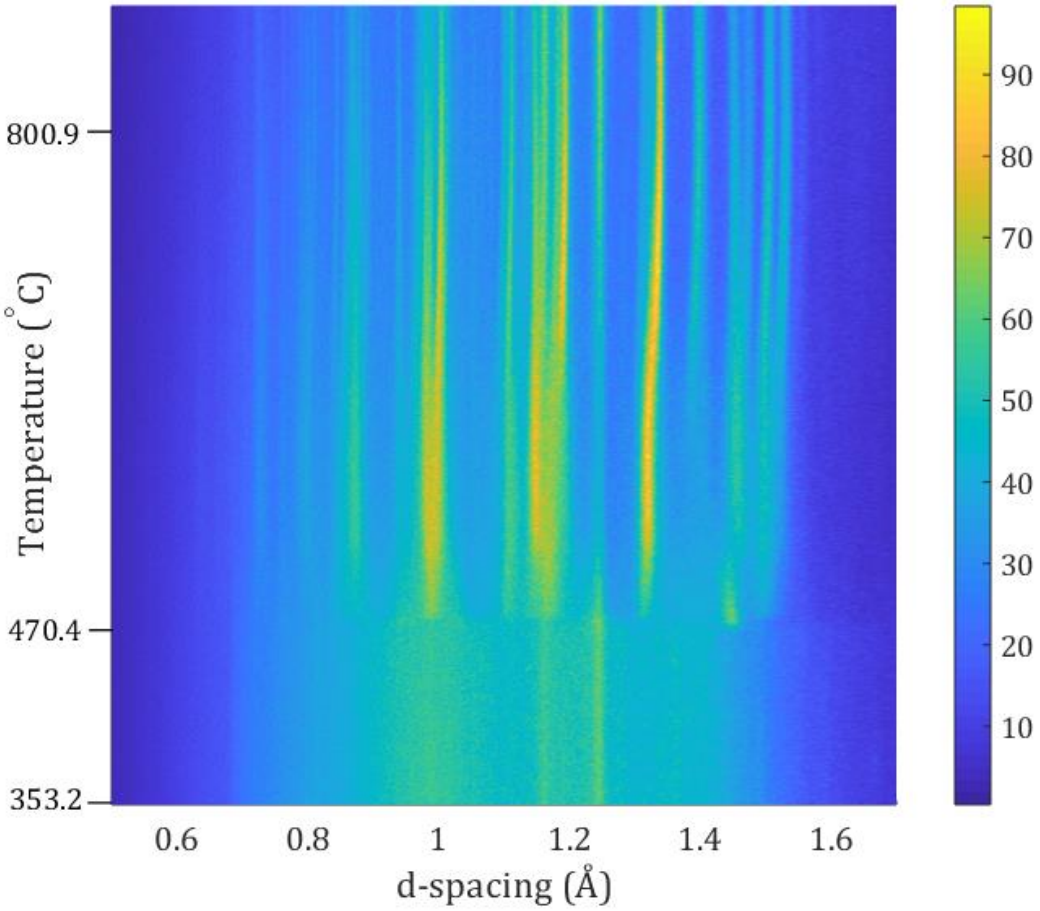

Figure 36. Bulk metallic glass sample, 999 stacked EDXD spectra, each with a 20 sec exposure time. Heating ramp starting temperature, sample crystallization temperature, and heating ramp final temperature are shown. Sample at 2.46 GPa at a heating rate of 1.2°C/min.

An example of how quickly the initial crystalline sample peaks appear is seen in Figure 37 where the bottom (in blue) line at 356.09°C is the spectrum from the start of the constant rate heating ramp, the orange line at 582.36°C is the spectrum immediately before the first new crystalline peaks are seen, the yellow line at 582.81°C is the first spectrum where evidence of sample crystallization is seen, and the purple line at 800.18°C is the spectrum at the end of the constant rate heating ramp, where many new crystalline peaks are seen.

Figure 37, along with Figure 36 show how unambiguous the decision of when crystallization occurred was.

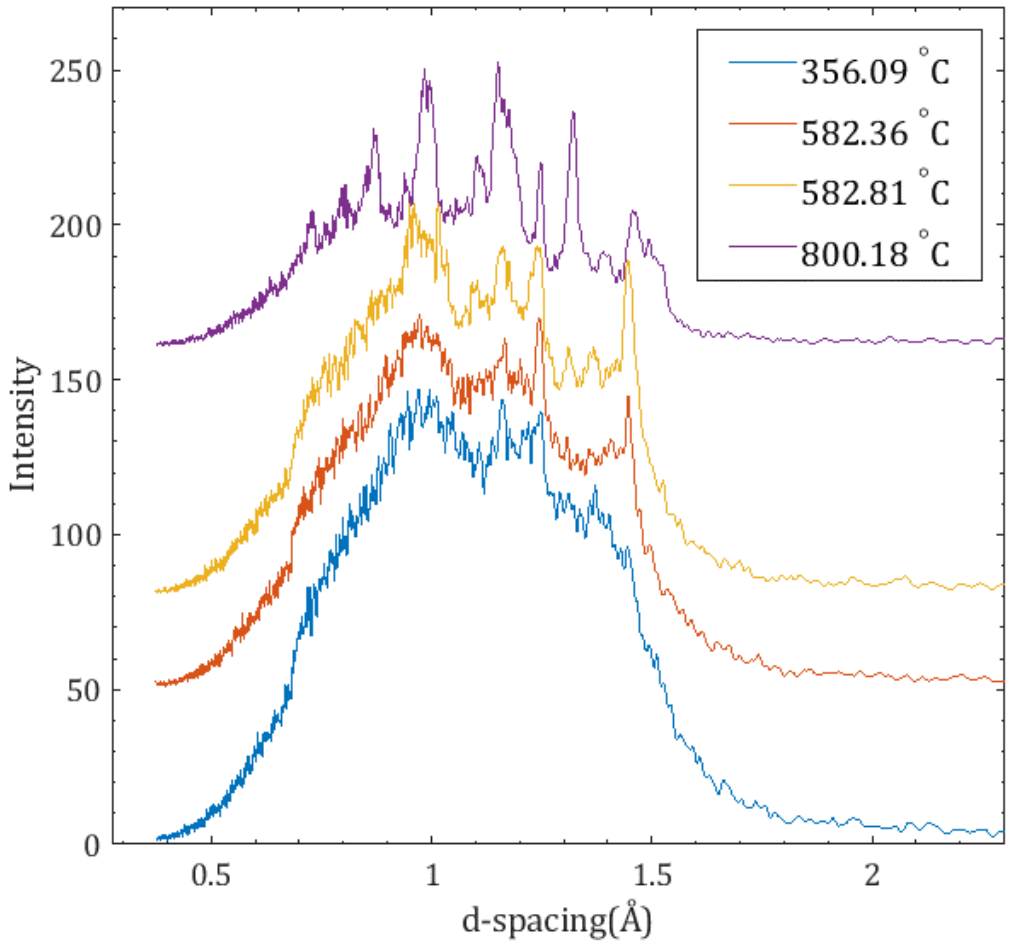

Figure 37. BMG sample at the beginning of the heating ramp, the spectrum immediately before evidence of crystallization, the spectrum with the first evidence of crystallization, and the end of the heating ramp.

The temperature where the first new crystalline peaks are seen is the temperature deemed the crystallization temperature, T_x. These crystallization temperatures are plotted in Figure

38. The EDXD measurements for crystallization temperature are consistent with the DSC measurements seen in Figure 38,Table 21 at ~0 GPa for the 6.0°C/min, 2.4°C/min, and 1.2°C/min heating rates.

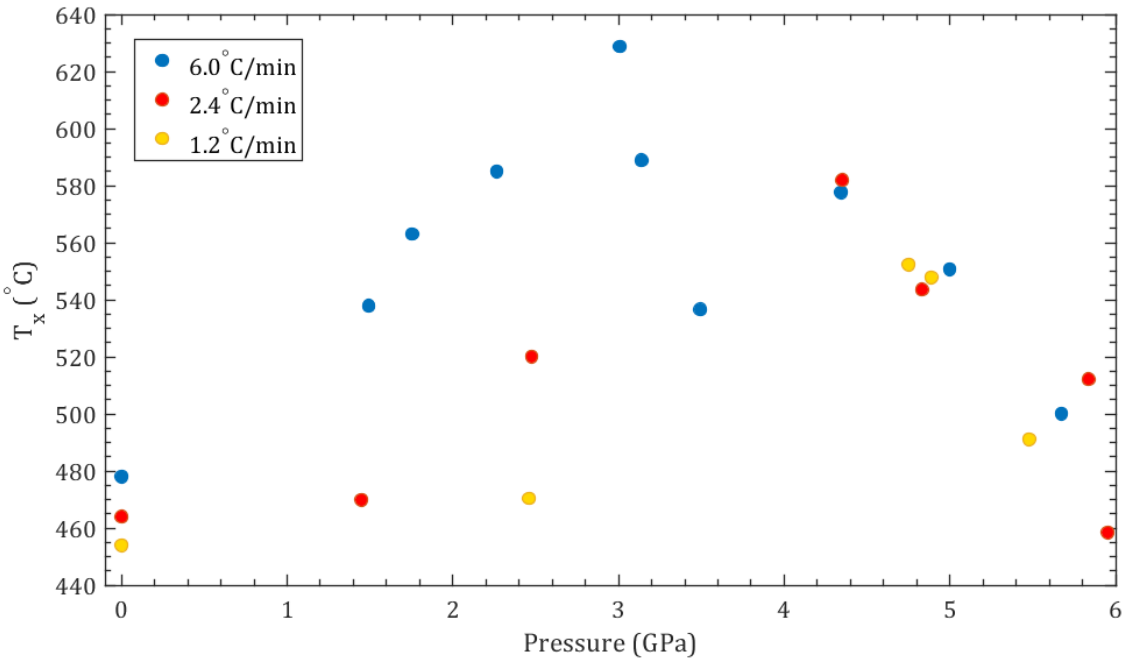

Figure 38. Crystallization temperature for three different constant heating rates.

Table 21. Crystallization temperatures for the three different heating rates. The temperatures with '*' were determined by DSC measurements.

6.0°C/min		2.4°C/min		1.2°C/min	
Pressure (GPa)	T_x (°C)	Pressure (GPa)	T_x (°C)	Pressure (GPa)	T_x (°C)
0	478*	0	464*	0	454*
1.49	538.0	1.45	469.9	2.46	470.4
1.75	563.2	2.47	520.1	4.75	552.4
2.26	585.0	4.35	582.0	4.89	547.8
3.01	628.7	4.83	543.6	5.48	491.1
3.14	588.9	5.84	512.2		
3.49	536.6	5.95	458.5		
4.34	577.6				

5.00	550.7
5.67	500.1

From this data it is seen that overall as the constant heating rate is increased, the crystallization temperature also increases. This effect is due to the dependence of atomic diffusion on heating rate. Since the crystallization of an amorphous compound relies on atomic diffusion, the faster the heating rate, the more difficult this process becomes which leads to an increased crystallization temperature [66]. Also, for all three heating rates there is a positive T_x trend vs pressure in the region of 1-3 GPa, and a negative T_x trend vs pressure in the region of 3-6 GPa (Figure 38, Table 21).

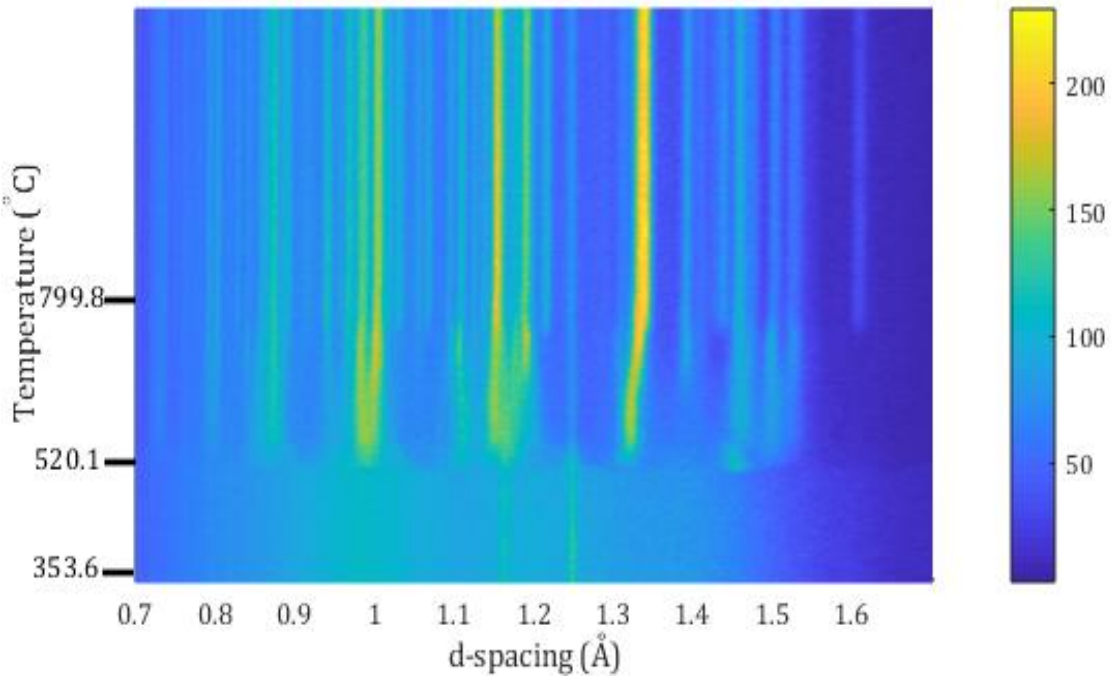

Figure 39. Constant heating rate run for Vit 106a at 2.47 GPa with a heating rate of 2.4°C/min

Table 22. Constant heating rate run for Vit 106a at 2.47 GPa with a heating rate of 2.4°C/min. The experimental d-spacing is compared to the calculated d-spacing for the equilibrium phases, and the crystallization temperature is also noted.

d-spacing (Å) (experimental)	Assignment	HKL	d-spacing (Å) (calc.)	Intensity (calc.)	T_x (°C)
1.607	**Zr_3Al_2**	3 3 2	1.600	30.57	747.7
	Zr_2Cu	2 0 0	1.609	16.37	
1.527	**Zr_2Ni**	3 3 0	1.529	8.89	520.1
	Zr_3Al_2	4 3 0	1.526	1.00	
1.501	Zr_4Al_3	1 1 3	1.499	14.02	520.1
	Zr_3Al_2	5 1 0	1.496	2.93	
	Zr_2Ni	2 1 3	1.505	34.42	
1.472	**Zr_3Al_2**	2 2 4	1.468	14.02	
1.456	Zr_2Ni	4 2 0	1.450	15.95	520.1
	ZrCu	2 1 0	1.459	78.16	
	Zr_2Cu	1 1 6	1.442	19.25	
	Zr_3Al_2	4 1 3	1.450	4.13	
1.437	**Zr_2Cu**	1 0 7	1.431	3.59	747.7
1.407	**Zr_2Cu**	0 0 8	1.398	0.75	747.7
1.392	Zr_3Al_2	4 3 2	1.399	1.54	695.7
	Zr_2Ni	4 0 2	1.382	14.44	
	Zr_2Cu	2 0 4	1.395	1.84	
1.336	Zr_2Ni	3 3 2	1.323	13.20	
	ZrCu	2 1 1	1.331	64.76	
	Zr_3Al_2	4 4 1	1.324	0.29	
1.310	Zr_3Al_2	5 2 2	1.314	8.78	520.1
	Zr_4Al_3	2 2 1	1.317	2.29	
1.250	**Zr_3Al_2**	2 2 5	1.242	2.58	520.1
1.240	Zr_3Al_2	6 1 1	1.235	0.88	
1.214	Zr_4Al_3	2 2 2	1.213	1.01	747.7
	Zr_3Al_2	3 1 5	1.211	4.03	
	Zr_2Cu	2 0 6	1.218	11.21	
1.190	Zr_4Al_3	3 0 3	1.182	6.60	695.7
	Zr_3Al_2	6 2 1	1.189	3.72	

1.176	Zr_2Ni	5 2 1	1.174	20.6	695.7
	Zr_3Al_2	5 4 1	1.175	1.53	
	Zr_4Al_3	3 1 2	1.175	26.8	
1.154	**ZrCu**	2 2 0	1.153	24.01	
1.137	**Zr_2Cu**	2 2 0	1.138	5.45	747.7
	Zr_3Al_2	5 1 4	1.137	1.73	
1.127	**Zr_3Al_2**	5 4 2	1.128	1.97	
1.108	**Zr_2Ni**	3 1 4	1.110	18.31	747.7
	Zr_3Al_2	2 1 6	1.104	6.22	
1.067	**Zr_3Al_2**	7 1 1	1.066	1.45	747.7
	Zr_2Cu	2 1 7	1.069	0.28	
1.054	Zr_2Cu	2 0 8	1.055	1.13	747.7
	Zr_2Ni	4 4 2	1.052	8.17	
	Zr_3Al_2	6 4 0	1.058	0.34	
	Zr_4Al_3	3 2 1	1.058	0.93	
1.029	**ZrCu**	3 1 0	1.031	37.97	747.7
	Zr_4Al_3	4 1 0	1.027	11.2	
	Zr_3Al_2	6 0 4	1.029	7.08	
	Zr_2Ni	5 3 2	1.025	15.48	
	Zr_2Cu	3 0 3	1.031	7.45	
1.015	Zr_3Al_2	6 4 2	1.013	6.01	747.7
	Zr_2Ni	5 3 2	1.025	7.72	
1.003	**Zr_4Al_3**	3 2 2	1.002	15.98	520.1
	Zr_3Al_2	7 3 0	1.002	2.26	
	Zr_2Ni	6 0 2	1.000	7.35	
0.988	**ZrCu**	3 1 1	0.983	34.32	520.1
	Zr_4Al_3	4 0 3	0.984	2.31	
	Zr_3Al_2	4 1 6	0.987	5.77	
0.981	Zr_4Al_3	2 0 5	0.980	2.28	
	Zr_3Al_2	3 3 6	0.979	7.79	
0.967	Zr_2Cu	3 0 5	0.967	0.18	695.7
	Zr_3Al_2	6 4 3	0.964	2.65	
0.954	**Zr_4Al_3**	2 2 4	0.957	14.79	695.7
	Zr_3Al_2	7 2 3	0.956	2.00	
	Zr_2Ni	6 2 2	0.956	13.35	

	Zr_2Cu	3 1 4	0.956	1.31	
0.939	**Zr_4Al_3**	3 1 4	0.937	0.64	695.7
	Zr_3Al_2	6 1 5	0.934	0.36	
	Zr_2Cu	0 0 12	0.932	0.57	
0.916	Zr_2Cu	2 0 10	0.918	1.32	
	Zr_2Ni	5 1 4	0.916	12.18	
	Zr_3Al_2	8 2 1	0.917	2.85	
0.907	Zr_3Al_2	5 4 5	0.907	1.33	
	Zr_4Al_3	3 3 0	0.906	3.73	
	ZrCu	3 2 0	0.905	28.71	
0.889	Zr_4Al_3	5 0 2	0.888	5.33	
	Zr_3Al_2	7 5 0	0.887	2.84	
	Zr_2Ni	0 0 6	0.880	1.40	
	Zr_2Cu	2 2 8	0.882	0.57	
0.875	Zr_4Al_3	4 2 1	0.877	3.03	
	Zr_3Al_2	4 1 7	0.880	1.03	
	Zr_2Ni	7 2 1	0.879	11.14	
	ZrCu	3 2 1	0.872	53.03	
0.869	Zr_3Al_2	7 3 4	0.869	2.28	
	Zr_2Ni	7 1 2	0.867	10.81	
	Zr_2Cu	3 2 3	0.868	1.72	
0.859	Zr_3Al_2	5 5 5	0.855	0.97	
	Zr_2Ni	6 4 2	0.851	10.41	
0.841	Zr_4Al_3	4 2 2	0.844	4.22	
	Zr_3Al_2	8 4 1	0.847	2.47	
	Zr_2Ni	6 3 3	0.847	10.30	

From this analysis it is seen that Zr_3Al_2 crystallizes at 520.1°C, Zr_4Al_3 crystallizes at 695.7°C, and Zr_2Cu crystallizes at 747.7°C (Figure 39, Table 22).

Rapid Heating and Cooling of Vit106a

The rapidly heated and cooled Vit 106a sample was brought to 4.2 GPa before heating. The sample went from 355°C → 800°C and 800°C → 224°C in 5 seconds. The sample then went from 224°C → 25°C in 20.1 seconds. Even with rapid heating and cooling the sample still crystallized (Figure 40), with peak assignments listed in Table 23.

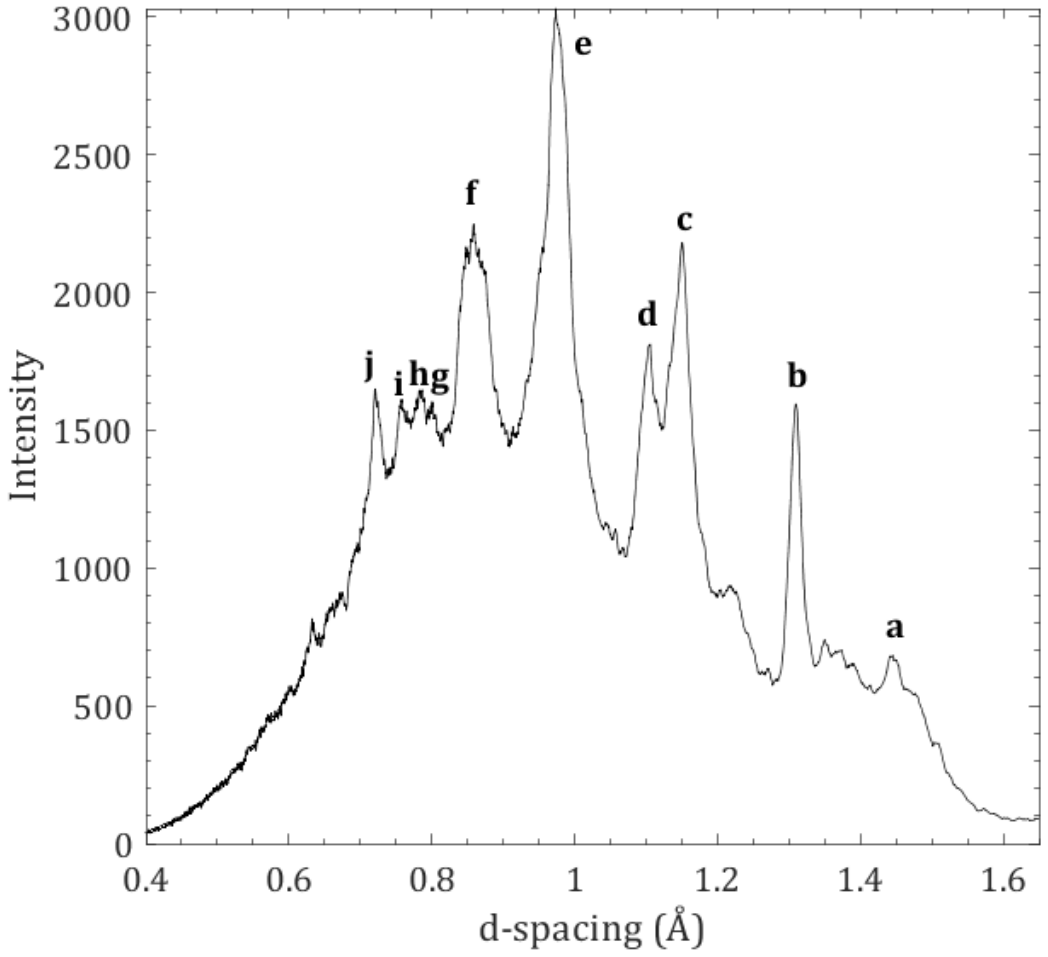

Figure 40. EDXD of rapidly heated and cooled sample of Vit 106a.

Table 23. Experimental EDXD peaks compared to calculated d-spacing for the crystalline phases of the rapidly heated and cooled Vit 106a sample. The assignments that are bold are the ones for each experimental d-spacing that have the highest calculated intensity.

Assignment	d-spacing (Å) (exp.)	Assignment	HKL	d-spacing (Å) (calc)	Intensity (calc.)
a	1.445	Zr_2Ni	4 2 0	1.45031	19.57
		ZrCu	2 1 0	1.4585	78.16
		Zr_2Cu	1 1 6	1.44165	19.25
		Zr_3Al_2	4 1 3	1.44975	4.13
b	1.309	Zr_3Al_2	5 2 2	1.31387	8.78
c	1.152	ZrCu	2 2 0	1.15304	24.01
d	1.103	ZrCu	3 1 0	1.03131	37.97
e	0.9739	Zr_3Al_2	3 3 6	0.97856	7.97
		Zr_2Ni	4 2 4	0.97621	13.96
		Zr_2Cu	2 2 6	0.97103	5.22
f	0.8587	Zr_3Al_2	5 5 5	0.85456	0.97
		Zr_2Ni	6 4 2	0.85139	10.41
g	0.8005	ZrCu	3 2 2	0.79098	21.47
		Zr_4Al_3	2 1 6	0.80184	7.41
		Zr_3Al_2	6 6 4	0.79975	2.42
h	0.783	Zr_2Ni	8 2 0	0.78654	4.38
		Zr_3Al_2	3 3 8	0.78663	0.16
		Zr_4Al_3	6 0 0	0.78419	3.64
i	0.7577	Zr_4Al_3	5 2 0	0.75342	3.97
		Zr_3Al_2	9 1 4	0.75914	1.58
		Zr_2Ni	7 5 0	0.75398	7.94
		Zr_2Cu	3 3 0	0.75849	1.31
j	0.721	Zr_2Cu	2 2 12	0.72082	0.87
		Zr_2Ni	5 1 6	0.72369	7.31
		Zr_3Al_2	9 1 5	0.72187	1.66

ZrCu	4 2 0	0.72925	17.94	

CONCLUSION

Quasi-hydrostatic compression of 17.6% boron-containing borosilicate glass was conducted to 13.7 GPa in a PE press at Beamline 16-BM-B, HPCAT, The Advanced Photon Source, Argonne National Laboratory. Multi-angle EDXD and white-beam radiography at a synchrotron source were utilized to obtain sample dimensions, reduced pair distribution function for the glass sample, and pressure variation of various bond distances. The radiography measurements revealed a permanent uniaxial contraction of 10.6% after decompression. From the reduced pair distribution function, the nearest neighbor Si–Si and second nearest neighbor Si–O bond lengths show evidence of permanent change indicating significant densification after pressurization. The bulk sample was recovered after compression to 13.7 GPa and the Raman spectroscopy experiments indicate blue-shift and intensity changes of Raman bands associated with silicate and four-coordinated boron. The increase in frequency of silicate rings indicate transition of 5- and 6-membered silicate rings to 4- and 5-membered silicate rings under compression.

Quasi-hydrostatic compression of a bulk metallic glass sample, $Zr_{58.5}Cu_{15.6}Ni_{12.8}Al_{10.3}Nb_{2.8}$ at ambient temperature was conducted to 4.91 GPa in a Paris-Edinburgh press. At 4.91 GPa the sample was heated to 800°C while held at a constant pressure. Multi-angle energy dispersive x-ray diffraction and white-beam radiography at a synchrotron source were utilized to obtain sample dimensions, reduced pair distribution function for the glass sample, and bulk sample volume. The radiography measurements revealed a 5.12% volume compression at ambient temperature and 4.91 GPa, and a volume compression of 14.94% at 800°C and 6.36 GPa from ambient pressure and temperature conditions. Evidence of crystallization is seen at 460°C from the volume collapse seen in

the radiography images. This is consistent with trends seen in the constant heating rate experiments.

The effect of pressure and heating rate on crystallization temperature was investigated for Vit 106a. A trend is seen for the heating rates investigated: 6.0°C/min, 2.4°C/min, and 1.2°C/min, where an increase in heating rate leads to an increase in crystallization temperature, and for each heating rate there is a positive correlation between pressure and crystallization temperature in a low-pressure range from ambient to ~3-4 GPa, and a negative correlation between pressure and crystallization temperature in a range from 3-4 GPa – 6.5 GPa. This is due to a reduction in atomic mobility via long-range diffusion for pressures up to ~3-4 GPa, and under higher pressures in the 3-4 GPa – 6.5 GPa range the free volume in the sample is reduced, leading to favored crystallization. In addition, the sample is seen to crystallize even under rapid heating and cooling, and thus an experimental critical heating rate is not found in this study.

Future work to expand on the work presented in this dissertation could include measurements on simpler Zr- based bulk metallic glass composition to determine what the limiting component is in the initial crystallization. Once determined, new Zr-based bulk metallic glass samples could be investigated, varying the composition of one component to test the effect it has on the crystallization temperature, with the goal of finding a bulk metallic glass that can go through to melt without devitrification.

REFERENCES

[1] P. J. Patel, A. J. Hsieh, G. A. Gilde, and A. P. Ground, *Improved Low-Cost Multi-Hit Transparent Armor* (2006).

[2] A. A. Wereszczak and C. E. Anderson, Int. J. Appl. Glas. Sci. **5**, 334 (2014).

[3] C. R. Kurkjian and W. R. Prindle, J. Am. Ceram. Soc. **81**, 795 (2005).

[4] L. A. B. Pilkington, Proc. R. Soc. A Math. Phys. Eng. Sci. **314**, 1 (1969).

[5] M. M. R. A. Lima, R. C. C. Monteiro, M. P. F. Graça, and M. G. Ferreira da Silva, J. Alloys Compd. **538**, 66 (2012).

[6] N. Bouras, M. A. Madjoubi, M. Kolli, S. Benterki, and M. Hamidouche, Phys. Procedia **2**, 1135 (2009).

[7] T. Kloss, G. Lautenschlaeger, and K. Schneider, Glas. Technol. **41**, 177 (2000).

[8] W. KLEMENT JUN., R. H. WILLENS, and P. O. L. DUWEZ, Nature **187**, 869 (1960).

[9] H. S. Chen, Acta Metall. **22**, 1505 (1974).

[10] A. J. Drehman, A. L. Greer, and D. Turnbull, Appl. Phys. Lett. **41**, 716 (1982).

[11] H. S. Chen and D. Turnbull, Appl. Phys. Lett. **10**, 284 (1967).

[12] H. S. Chen, J. T. Krause, and E. Coleman, J. Non. Cryst. Solids **18**, 157 (1975).

[13] A. Inoue, T. Zhang, and T. Masumoto, Mater. Trans. JIM **30**, 965 (1989).

[14] A. Inoue, T. Zhang, and T. Masumoto, Mater. Trans. JIM **31**, 177 (1990).

[15] T. Zhang, A. Inoue, and T. Masumoto, Mater. Trans. JIM **32**, 1005 (1991).

[16] L. Wang and A. Inoue, Mater. Trans. **42**, 2637 (2001).

[17] A. Inoue, A. Takeuchi, and B. Shen, Mater. Trans. **42**, 970 (2001).

[18] A. L. Greer, Nature **366**, 303 (1993).

[19] A. Inoue, Acta Mater. **48**, 279 (2000).

[20] M. Telford, Mater. Today **7**, 36 (2004).

[21] Q. Chen, L. Liu, and S.-M. Zhang, Front. Mater. Sci. China **4**, 34 (2010).

[22] K. Imai, J. Mater. Sci. Chem. Eng. **04**, 46 (2016).

[23] W. He, A. Chuang, Z. Cao, and P. K. Liaw, Metall. Mater. Trans. A **41**, 1726 (2010).

[24] J. Li, L. Shi, Z. Zhu, Q. He, H. Ai, and J. Xu, Mater. Sci. Eng. C **33**, 2113 (2013).

[25] S. E. Naleway, R. B. Greene, B. Gludovatz, N. K. N. Dave, R. O. Ritchie, and J. J. Kruzic, Metall. Mater. Trans. A **44**, 5688 (2013).

[26] W. L. Johnson, JOM **54**, 40 (2002).

[27] E. M. Axinte and M. P.I. Chirileanu, Recent Patents Mater. Sci. **5**, 213 (2012).

[28] L. J. Kecskes, B. T. Edwards, and R. H. Woodman, in *Transform. Sci. Technol. Curr. Futur. Force* (WORLD SCIENTIFIC, Aberdeen Proving Ground, 2006), pp. 257–263.

[29] D. R. Siddle and C. D. Dunn, 8,171,851 B2 (2012).

[30] W. Resistance and S. Properties, (2017).

[31] B. D. Cullity, *Elements of X-Ray Diffraction* (AddisonWesley Publishing Company, Inc., Massachusetts, 1978).

[32] C. Suryanarayana and M. G. Norton, *X-Ray Diffraction* (Springer US, Boston, MA, 1998).

[33] Y. Kono, C. Park, C. Kenney-Benson, G. Shen, and Y. Wang, Phys. Earth Planet. Inter. **228**, 269 (2014).

[34] Y. Fei, J. Li, K. Hirose, W. G. Minarik, J. a. Van Orman, C. Sanloup, W. van Westrenen, T. Komabayashi, and K. Funakoshi, Phys. Earth Planet. Inter. **143**–**144**, 515 (2004).

[35] S. H. Shim, T. S. Duffy, and K. Takemura, Earth Planet. Sci. Lett. **203**, 729 (2002).

[36] B. E. Warren, J. Am. Ceram. Soc. **75**, 5 (1992).

[37] S. Billinge, *Pair Distribution Function Technique: Principles and Methods* (2012).

[38] C. Norman, L. Daly, and S. Wiberley, *Introduction to Infrared and Raman Spectroscopy*, 2nd ed. (Academic Press, New York, 1975).

[39] E. Smith and G. Dent, *Modern Raman Sectroscopy - A Practical Approach* (2005).

[40] A. Smekal, Naturwissenschaften **11**, 873 (1923).

[41] C. V. Raman and K. S. Krishnan, Nature **121**, 501 (1928).

[42] R. J. Hemley, H. K. Mao, P. M. Bell, and B. O. Mysen, Phys. Rev. Lett. **57**, 747 (1986).

[43] B. G. Parkinson, D. Holland, M. E. Smith, C. Larson, J. Doerr, M. Affatigato, S. A. Feller, A. P. Howes, and C. R. Scales, J. Non. Cryst. Solids **354**, 1936 (2008).

[44] W. L. Konijnendijk and J. M. Stevels, J. Non. Cryst. Solids **20**, 193 (1976).

[45] O. N. Koroleva, L. A. Shabunina, and V. N. Bykov, Glas. Ceram. (English Transl. Steklo i Keramika) **67**, 340 (2011).

[46] G. S. Smith and L. E. Alexander, Acta Crystallogr. **16**, 462 (1963).

[47] K. J. Ham, Y. K. Vohra, Y. Kono, A. A. Wereszczak, and P. Patel, High Press. Res. **0**, 1 (2017).

[48] K. Persson, (2014).

[49] Y. Kono, T. Irifune, Y. Higo, T. Inoue, A. Barnhoorn, D. Suetsugu, C. Bina, T. Inoue, D. Wiens, and M. Jellinek, Phys. Earth Planet. Inter. **183**, 196 (2010).

[50] M. Fábián, E. Sváb, T. Proffen, and E. Veress, J. Non. Cryst. Solids **354**, 3299 (2008).

[51] H. Inoue, A. Masuno, and Y. Watanabe, J. Phys. Chem. B **116**, 12325 (2012).

[52] L. Pedesseau, S. Ispas, and W. Kob, Phys. Rev. B - Condens. Matter Mater. Phys. **91**, 1 (2015).

[53] D. Möncke, G. Tricot, D. Ehrt, and E. I. Kamitsos, J. Chem. Technol. Metall. **50**, 381 (2015).

[54] S. Reich, a. Ferrari, R. Arenal, a. Loiseau, I. Bello, and J. Robertson, Phys. Rev. B **71**, 1 (2005).

[55] A. K. Stemshorn, Y. K. Vohra, and S. J. Smith, J. Appl. Phys. **123**, 215901 (2018).

[56] M. W. Guinan, D. N. Beshers, and H. Krumb, J. Phys. Gem. Solids Pergamon Press **29**, 541 (1968).

[57] Y. Inamura, Y. Katayama, and W. Utsumi, J. Phys. Condens. Matter **19**, 415104 (2007).

[58] C. Meade, R. J. Hemley, and H. K. Mao, Phys. Rev. Lett. **69**, 1387 (1992).

[59] Cambridge University Engineering Department, Mater. Courses 1 (2003).

[60] D. Ma, A. D. Stoica, X.-L. Wang, Z. P. Lu, and T. Proffen, Appl. Phys. A Mater. Sci. Process. **99**, 537 (2010).

[61] L. Shadowspeaker, M. Shah, and R. Busch, Scr. Mater. **50**, 1035 (2004).

[62] H. LIPSON, *Structure Types. Part 10: Space Groups (140) I4/Mcm – (136) P42/Mnm* (Springer Berlin Heidelberg, Berlin, Heidelberg, 2011).

[63] P. Villars, K. Cenzual, J. Daams, R. Gladyshevskii, O. Shcherban, V. Dubenskyy, N. Melnichenko-Koblyuk, O. Pavlyuk, S. Stoiko, and L. Sysa, in *Struct. Types. Part 3 Sp. Groups P63/Mmc - P-62c*, edited by P. Villars and K. Cenzual (Springer-Verlag, Berlin/Heidelberg, 2006), pp. 1–1.

[64] F. Aubertin, S. J. Campbell, and U. Gonser, Hyperfine Interact. **28**, 997 (1986).

[65] A. V. Zhalko-Titarenko, M. L. Yevlashina, V. N. Antonov, B. Y. Yavorskii, Y. N. Koval, and G. S. Firstov, Phys. Status Solidi **184**, 121 (1994).

[66] S. Zhang, T. Ichitsubo, Y. Yokoyama, T. Yamamoto, E. Matsubara, and A. Inoue, Mater. Trans. **50**, 1340 (2009).